Control Strategies Impacts during Low-Level Jet Events on a 15MW Floating Wind Turbine

Tord Nyland Malmei

Thesis for Master of Science Degree at the
University of Bergen, Norway

2024

Year: 2024
Title: Control Strategies Impacts during Low-Level Jet Events on a 15MW Floating Wind Turbine
Author: Tord Nyland Malmei

Acknowledgements

I would like to express my gratitude to my supervisor, Mostafa Bakhoday Paskyabi, for his guidance and support throughout my studies. His expertise in the field and the engineering mindset have been invaluable. I would also like to extend my gratitude to my fellow students for the five years we spent together on the integrated master's in energy. I'd like to thank my family for all their support.

Abstract

The size and complexity of wind turbines are increasing as the energy demand continues to grow. Offshore wind energy has significant potential, and the floating 15MW wind turbine has become the new standard in the venture. Offshore placement of wind turbines results in new interactions between the turbines and transient weather events. Wind turbine control strategies are crucial for enhancing wind turbines' performance, reliability, and durability during operation. This study aims to investigate the effect of different control strategies on the performance of a 15MW floating turbine during Low-Level Jets (LLJ). The control strategies that have been investigated include collective pitch control, individual pitch control (IPC), peak shaving (PS), tip speed ratio (TSR) tracking torque control, and constant power tracking torque control. The Reference Open-Source Controller (ROSCO) was used to set up the controller, while OpenFAST simulation software was used to generate the turbine response. TurbSim was used to generate turbulent winds. The results showed that different control strategies highly impact the wind turbine performance during an LLJ. It is also evident that there are variations in the results depending on the height of the LLJ. IPC was the most effective in mitigating the greatest number of loads without reducing the power extraction. It appears that TSR tracking torque control is sub-optimal during LLJs regarding power extraction.

Contents

Chapter 1

Introduction

1.1 Motivation

According to the report Bouckaert et al. (2021), the share of renewable energy must increase from under 30% of the electricity supply in 2020 to nearly 70% in 2050 to achieve net zero carbon emissions in the global energy sector by 2050. Solar and wind power are projected to account for almost half of the world's electricity supply by 2050 (Bouckaert et al., 2021). To make this achievable, the European Commission has structured a European Wind Energy Action Plan to ensure a healthy, sustainable, and competitive wind supply chain (European Commission, 2023). The plan is divided into six main pillars. One of the pillars for developing the sector is acquiring new skills (European Commission, 2023). Floating offshore wind is still in its early stages and will require a high level of knowledge to realise its potential in the coming years and decades. Harsh environmental offshore conditions and large wind turbines present new technological, technical, and research challenges (Bakhoday-Paskyabi & Flügge, 2021). When placing a multi-million structure in these conditions, it is crucial to consider sustainability and durability. Adapting wind turbines to environmental conditions can reduce maintenance costs and increase sustainability.

1.2 Problem Statement and Objectives

Harsher environmental conditions require better-designed and adapted wind turbine operation. In addition to increased wind speeds and waves, it is

important to consider the impact of transient weather events like Low-Level Jets (LLJ). LLJ are characterised by a core where the horizontal wind speed is at its highest magnitude. The wind profile under the core has positive shear, while over the core, there is a decreasing wind speed with height, known as negative shear. Wind turbines must be able to handle both positive and negative shear simultaneously when the LLJ core height is within the rotor area. This forms the main research question of this thesis: *Understand the impact of control strategies on the performance of a 15MW Floating Offshore Wind Turbine (FOWT) during a low-level jet event.* This study evaluates the performance of the wind turbine in terms of power generation, aerodynamic loads, and structural loads. To achieve this objective, the study will investigate low-level jet cases with different core heights and core wind speeds in combination with different control strategies. The Reference Open-Source Controller (ROSCO) will be used to configure the controller setup, while the engineering simulation software OpenFAST will generate the turbine response. Turbulent wind will be generated as input to OpenFAST using the TurbSim software. The research will investigate both ideal and observed cases of low-level jets.

Contribution

This study aims to contribute to the knowledge-building part of the offshore wind venture in terms of the interaction between transient weather events and wind turbines. The thesis also contributes on a personal level by increasing my engineering skills through the use of simulation tools (TurbSim, OpenFAST) and increasing my knowledge of control systems and the dynamics of a wind turbine. It has also contributed to my engineering mindset through data processing and -analysis in Python.

Chapter 2

Theory

This chapter presents the theoretical background necessary to comprehend the offshore environmental conditions, the dynamics of floating offshore wind turbines, the fundamentals of control systems, and the principles of different control strategies. The first section comprises a literature review on the subject.

2.1 Literature review

A study by Ahmed (2023) investigated the effect of low-level jet heights on the structural loading of a 15MW floating wind turbine. He found that there was a non-trivial interaction between the structure and the wind profile and that there were no unique patterns in the way the loads developed. The results showed that the mean hub velocity affected the load response and the shear influenced the aerodynamic loads along the blades. The effect of control was not investigated in this study. A study by Gutierrez et al. (2017) examined the effect of negative wind shear within the swept area of the rotor and found that the presence of negative wind shear positively affected reducing nacelle and tower movements in all directions. Only the spanwise movements of the tower was increased by the negative shear, but this occurred at the slower velocities and accelerations of the tower. Based on the results, the study suggested that larger wind turbines with the rotor within the negative shear of an LLJ would be beneficial with minimal external shear loads.

There are many different control strategies. The paper by Njiri & Söffker (2016) provides an overview of different control strategies and discusses

emerging trends in the control of wind turbines. The authors write that different control strategies reduce different structural loads. Individual Pitch Control (IPC) can reduce the side-side tower deflection and mitigate rotor blade loads. Meanwhile, Collective Pitch Control (CPC) can minimize tower fore-aft deflection. The studies by Bossanyi (2003b) and Lara et al. (2023) investigated the benefits of IPC. Both studies indicate that IPC results in a significant reduction in operational loads. Lara et al. (2023) results indicated that IPC reduced the out-of-plane blade moment without sacrificing power generation but at the cost of increased pitch actuator effort. Wang et al. (2024) conducted a study on advanced turbine control strategies using a model-scale floating offshore wind turbine system. The study investigated the effect of thrust Peak Shaving (PS) by pitch saturating using ROSCO. The results indicated that PS reduced the peaks in thrust and tower fore-aft motion. However, it had some issues with thrust variations caused by wave-excited platform motion. To date, it has not been possible to identify any studies that have investigated the control strategies efficiency previously mentioned in conjunction with low-level jets.

2.2 The offshore environmental conditions

Offshore wind turbines operate in a dynamic and challenging environment, influenced by wind, waves, and currents. Unlike the wind over land, the boundary between waves and wind determines the roughness of the surface, which is dependent on the wave height. The temperature differences between sea and air and land and air follow different patterns over time, resulting in a different wind field offshore. Therefore, when it comes to offshore wind turbines, the experience from onshore wind turbines has some limitations (Nielsen, 2024). These environmental conditions significantly impact offshore wind turbine design, operation, and maintenance. Strong and consistent offshore winds offer substantial potential for renewable electricity generation but also present engineering challenges. Offshore waves and currents can impact the stability and performance of turbine structures, making it crucial to understand and manage these environmental conditions to maximise the efficiency and reliability of offshore wind energy production.

2.2.1 Atmospheric Boundary Layer

The region between the ground or sea surface and the 'free' atmosphere is called the Atmospheric Boundary Layer (ABL) (Nielsen, 2024). The effect of surface friction on the wind field can be ignored in the free atmosphere. Between the free atmosphere and the ABL, there is an inversion layer that limits the exchange of air between the two (Garratt, 1994). The lowest 10% (50 – 100m) of the ABL is referred to as the surface layer. In this layer, the vertical shear is approximately constant and buoyancy effects from temperature and surface friction determine the wind structure (Kaimal & Finnigan, 1994). In general, wind turbines are known to operate in the surface layer of the atmosphere. However, the new, large offshore turbines may operate above this height and more into the upper part of the atmospheric boundary layer. The wind structure in the upper part of ABL is significantly impacted by the Coriolis effect (Kaimal & Finnigan, 1994). This causes a consistent change in the mean wind direction within the boundary layer. In the field of wind engineering, the Coriolis effect is frequently neglected, with only the surface layer being considered for simplicity (Nielsen, 2024).

Turbulence

The mean wind velocities can be divided into one mean component and one fluctuating stochastic component:

$$u = \bar{u} + u', \tag{2.1}$$

$$v = \bar{v} + v', \tag{2.2}$$

$$w = \bar{w} + w', \tag{2.3}$$

where bar denotes mean and " $'$ " denotes fluctuating. The turbulence intensity for the u-component of wind is given by (Bhattacharya, 2019):

$$TI = \frac{\sigma_u}{\bar{u}}, \tag{2.4}$$

where σ_u is the standard deviation of the velocity fluctuations (Bhattacharya, 2019). The turbulence intensity also depends on the site location, and surface roughness length and is influenced by the wind turbine itself (Bhattacharya,

2019). In the context of wind engineering, it is typically the fluctuations and turbulence intensity in mean wind velocity that are considered (Nielsen, 2024). The surface roughness length, denoted z_0, depends on the wind speed, distance to shore and the wave conditions offshore. Nielsen (2024). For open sea conditions, the roughness length is in the range of 0.0001 for calm water to 0.01 for rough waves (Dnv, 2014).

Kaimal wind spectrum

The fluctuations of the wind at one point are typically described using the Power Spectral Density (PSD) spectrum, also known as the wind spectrum. This spectrum describes how the power of the wind is distributed in the frequency domain. In wind engineering, the most popular wind spectrum is the Kaimal spectral model Kaimal et al. (1972):

$$\frac{fS_u}{u_*^2} = \frac{105 f_r}{(1+33 f_r)^{5/3}}, \tag{2.5}$$

$$\frac{fS_v}{u_*^2} = \frac{17 f_r}{(1+9.5 f_r)^{5/3}}, \tag{2.6}$$

$$\frac{fS_w}{u_*^2} = \frac{2.1 f_r}{(1+5.3 f_r)^{5/3}}, \tag{2.7}$$

$$\frac{fReS_{uw}}{u_*^2} = -\frac{14 f_r}{(1+9.6 f_r)^{7/3}}, \tag{2.8}$$

where $f_r = \frac{fz}{\bar{u}}$ is a dimensionless frequency, $S_u(f)$, $S_v(f)$, $S_w(f)$ and $S_{uw}(f)$ are the wind spectrum (Kaimal et al., 1972).

Davenport coherence model

When computing wind loads on a wind turbine, it is important to consider not only the velocity variations at one point (wind spectrum) but also the spatial velocity variations (Nielsen, 2024). The coherence of a wind field indicates the correlation between wind speeds at different points. It measures how much the variation in wind speed at one point is related to the wind speed at another point. Due to the new rotor sizes that exceed 200 meters, variations in u-velocity are of significant importance. The coherence between two horizontal points and two vertical points differs mainly due to the vertical

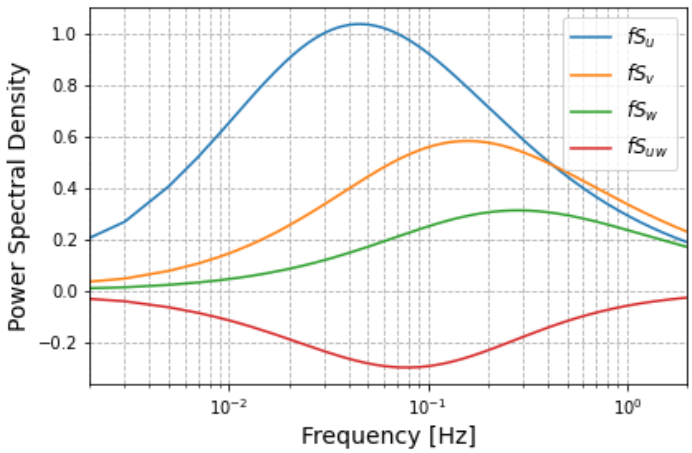

Figure 2.1: Example of Kaimal wind spectrum S_u, S_v and S_w, and co-spectrum between u and w, S_{uw}.

shear in the mean wind profile, but also the thermodynamic effects due to temperature difference (Nielsen, 2024). Consider two positions y_1 and y_2, where the auto-spectra for the wind are denoted $S_{y_1y_1}(f)$, $S_{y_2y_2}(f)$ and the cross-spectrum $S_{y_1y_2}(f)$ the coherence are given by Nielsen (2024):

$$\gamma(y_1, y_2, f) = \frac{S_{y_1y_2}(f)}{\sqrt{S_{y_1y_1}(f)S_{y_2y_2}(f)}}. \tag{2.9}$$

Coherence consists of one real part denoted co-coherence and one imaginary part denoted quad-coherence. In wind engineering the imaginary part is discarded and only the real part is considered (Nielsen, 2024)

The Davenport coherence model is the most commonly used model for wind-load estimation (Cheynet et al., 2018). Davenport (1961) demonstrated that vertical coherence can be modelled effectively when the separation is small compared to the typical length scale of the turbulence (Cheynet et al., 2018). The model was later extended by Pielke & Panofsky (1970) to be valid for horizontal coherence and it is given by (Cheynet et al., 2018):

$$\gamma_i(z_1, z_2, f) = \exp\left(-\frac{c_1^i f|z_1 - z_2|}{0.5(\bar{u}(z_1) + \bar{u}(z_2)}\right), \tag{2.10}$$

where z_1 and z_2 are two spatial points, c_1^i is a decay coefficient, and $i = u, v, w$ Cheynet et al. (2018).

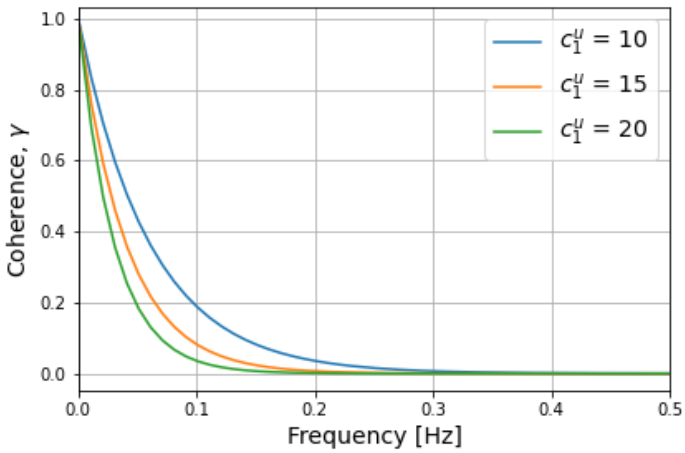

Figure 2.2: Example of Davenport coherence model. Equation (2.10) plotted with 12 m/s mean wind speed, horizontal distance 20 meters and different decay coefficients, c_1^u.

2.2.2 Wind profiles

There are various methods to describe the flow field in the atmospheric boundary layer. The Navier-Stokes equation can describe the flow field using a Cartesian coordinate system with $(x,y,z) = (u,v,w)$, where u represents the mean wind velocity, v is the transverse velocity, and z is the vertical velocity. The mean velocity in the transverse and vertical directions is assumed to be zero. By assuming a neutral stability of the atmosphere and a constant turbulent flux in the vertical direction the logarithmic wind profile is obtained (Nielsen, 2024):

$$\bar{u}(z) = \frac{u_*}{\kappa} \ln\left(\frac{z}{z_0}\right), \tag{2.11}$$

where $\bar{u}(z)$ is the mean wind speed at height z, u_* is the friction velocity, κ is the von Kàrmàn constant that is equal 0.4 and z_0 is the roughness length (Nielsen, 2024).

In engineering applications, the simpler power law is often used instead of the logarithmic wind profile, which gives the 10-minute average wind

velocity at the vertical level z. The power law is written as (Nielsen, 2024):

$$U_{10}(z) = U_r \left(\frac{z}{z_r} \right)^{\alpha}, \tag{2.12}$$

where U_r is the reference wind speed at the reference height z_r and α is the power law exponent that is obtained by (Nielsen, 2024):

$$\alpha(z) = \frac{ln(\frac{ln(z/z_0)}{ln(z_r/z_0)})}{ln(z/z_r)}. \tag{2.13}$$

2.2.3 Low-level jet phenomena

Low-level jet occurrences were first recorded over the southern Great Plains of the USA. LLJs were of interest as phenomena in themselves and their effects on weather and weather-related activities, such as the development of thunderstorms, aircraft operations and the spread of forest fires (Bonner, 1968). The phenomena of LLJ have later been discovered both over land and sea (Wagner et al., 2019), and are now of interest in wind energy technology.

Low-level jets are generated by two main mechanisms: Inertial Oscillations (IO) and baroclinicity can cause the phenomenon, either individually or in combination (Wagner et al., 2019; Bakhoday-Paskyabi et al., 2022). The driving mechanisms often vary depending on location (Wagner et al., 2019). Blackadar (1957) explains the occurrence of LLJ to be strongly associated with thermal inversion (often nocturnal inversion) and IO, and to occur with a diurnal cycle. Central to the explanation is the frictional decoupling that occurs between the boundary layer and the overlying flow due to the thermal inversion. The imbalance between the Coriolis and pressure gradient forces, results in an inertial oscillation with a period of $2\pi/f$, where f is the Coriolis force (Bakhoday-Paskyabi et al., 2022). Initially, the wind is subgeostrophic, but after less than half the inertial period it becomes supergeostrophic (Bakhoday-Paskyabi et al., 2022). Blackadar (1957) also found a strong relationship between the height of the inversion layer and the height of the low-level jet.

Holton (1967) first discussed the generation of low-level jets due to baroclinicity, which is the effect of temperature and pressure on density. These

jets occurred due to a horizontal temperature gradient in sloping terrain and changed direction and magnitude with a diurnal cycle (Holton, 1967). The horizontal temperature gradient can also occur in the land-sea interface or by a cyclone-induced cold front (Bakhoday-Paskyabi et al., 2022). A steep slope of the isobaric surfaces results from a strong temperature gradient zone near the surface. The thermal wind relation leads to a high maximum of the geostrophic wind speed at the surface, which decreases with increasing height. The LLJ is caused by a decrease in geostrophic wind height above it and a decrease in wind due to friction below it (Bakhoday-Paskyabi et al., 2022).

The study by De Jong et al. (2024) reported that in the U.S. Mid-Atlantic offshore region, the LLJs occurred due to horizontal temperature gradients that arise from the land-sea breeze, which forces warmer air over the cold ocean surface, and from fronts and synoptic systems. Wagner et al. (2019) reported that the LLJs in the North Sea region were formed by both IOs and baroclinic effects, which is in accord with Bakhoday-Paskyabi et al. (2022) who pointed out that the occurrence of a strong IO-produced LLJ requires a relatively strong geostrophic wind in the first place. The study by Wagner et al. (2019) revealed that the average low-level jet core height was 236 metres and the average core speed was 11.8 m/s over the Southern North Sea.

2.2.4 Ocean waves

Phillips (1957) found that the generation of waves by the wind starts with small waves with wavelengths of a few centimetres, generated by the random pressure fluctuations in the turbulent wind. The wave profile then leads to pressure differences as the wind passes, resulting in growing waves. The waves grow exponentially due to the larger wave/larger pressure difference ratio (Miles, 1957). At this stage the waves begin to interact with themselves, resulting in longer waves (Hasselmann et al., 1973).

2.2.5 Linear wave theory

Linear wave theory is generally used to describe wave characteristics because of its simplicity when calculating loads on marine structures. The

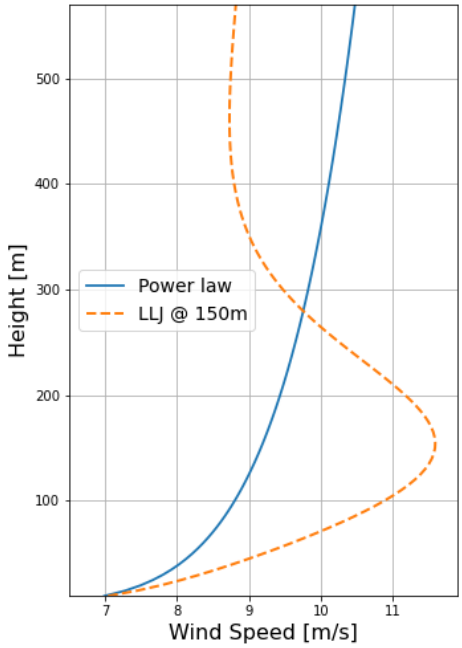

Figure 2.3: Comparison of the power law wind profile (solid blue line) and a low-level jet (dashed orange line).

characteristics of waves are denoted by a set of parameters. Wavelength: λ, wave number: $k = \frac{2\pi}{\lambda}$, angular frequency: $\omega = \frac{2\pi}{T}$, wave period: $T = \frac{2\pi}{kc}$, phase speed (travel speed of wave crest): $c = \frac{\omega}{k}$ (Kundu et al., 2015). The surface elevation of the monochromatic wave is described by (Kundu et al., 2015):

$$\eta(x,t) = a\cos(kx - \omega t), \tag{2.14}$$

where a is the amplitude of the wave.

The linear wave theory is based on the assumption of an ideal fluid (incompressible, no viscous effects, constant density and irrotational), meaning there are no internal waves in the fluid. The velocity field can then be described by a velocity potential, where the fluid velocities are the gradients of the velocity potential (Kundu et al., 2015):

$$\mathbf{u} = \nabla\phi, \tag{2.15}$$

where **u** is the velocity vector (u, v, w) corresponding to the velocity in x, y and z direction. Based on the assumptions of an incompressible and irrotational fluid, the velocity potential satisfies the Laplace equation given by (Kundu et al., 2015):

$$\nabla^2\phi = \frac{\delta^2\phi}{\delta x^2} + \frac{\delta^2\phi}{\delta y^2} + \frac{\delta^2\phi}{\delta z^2} = 0. \tag{2.16}$$

The theory is derived by three boundary conditions and by choosing the wave direction to be in the x-direction, which implies that the horizontal velocity in y-direction is zero. The three boundary conditions are (Kundu et al., 2015):

- At bottom boundary condition: zero vertical velocity at the bottom of the sea.
- Kinematic boundary condition: implies that particles once located at the free surface will remain there.
- Dynamic boundary condition: pressure on the free surface equals the atmospheric pressure.

It is assumed that the slope of the waves is small and that the dynamic and kinematic boundary conditions are satisfied at $z = 0$ rather than at η to obtain a linear solution. By using the bottom kinematic boundary condition and assuming that the solution should represent a harmonic progressive wave, a solution of the Laplace equation is derived (Kundu et al., 2015):

$$\phi = \frac{a\omega}{k}\frac{\cosh(k(z+h))}{\sinh(kH)}\sin(kx - wt) \tag{2.17}$$

By using the dynamic boundary condition a relationship between ω and k, the dispersion relation is derived:

$$\omega^2 = gk\tanh(kh) \tag{2.18}$$

By substituting the dispersion relation into the equation of phase speed, the fundamental result is derived and given by (Kundu et al., 2015):

$$c = \frac{\omega}{k} = \sqrt{\frac{g}{k}\tanh(kh)} \tag{2.19}$$

This shows that surface waves are dispersive because their propagation speed is dependent on the wave number. The physical interpretation of the results is that waves with longer wavelengths travel faster than waves with shorter wavelengths (Kundu et al., 2015).

2.2.6 JONSWAP wave spectrum

Offshore locations are comprised of numerous waves with varying frequencies and wavelengths. The significance of each frequency is determined by its associated power (Bhattacharya, 2019). The JONSWAP (Joint North Sea Wave Project) spectrum is used to describe wind-generated waves in deep water and has been developed from extensive measurements of wave data in the North Sea region. The project discovered that the wave spectrum does not fully develop but evolves over long distances and periods through non-linear wave-to-wave interactions (Hasselmann et al., 1973). The JONSWAP spectrum is a widely used model in offshore and coastal engineering for predicting ocean characteristics and wave conditions.

2.3 Wind turbines

Wind turbines convert the wind's kinetic energy into mechanical (rotational) energy, which a generator transforms into electricity. The Horizontal Axis Wind Turbine (HAWT) is the most commonly used type of wind turbine. However, there are also Vertical-Axis Wind Turbines (VAWT) that rotate around the vertical axis. The HAWT consist of a tower with a Rotor Nacelle Assembly (RNA) at the top of the tower. The RNA consists of the nacelle where the control system, generator, gearbox and shafts are placed. The nacelle is connected to the hub to which the blades are connected. The RNA can rotate at the top of the tower, a process known as yawing. This ensures that the rotor plane faces the incoming wind. (Nielsen, 2024)
Wind power is determined by the amount of mass passing through a cross-sectional area per unit of time. The power in wind is given by (Nielsen,

2024):

$$P = \frac{1}{2}\rho A_r U^3 \tag{2.20}$$

where ρ is the air density, A_r is the cross-sectional area of the rotor, and $U = \sqrt{u^2 + v^2}$ is the horizontal wind speed. Thus the power in wind is proportional to the cube of the wind speed. However, it is impossible to extract all of the kinetic energy because the wind would then have no velocity behind the rotor, causing it to pile up. The theoretical maximum power extracted by a wind turbine, derived by Albert Betz in 1919 and referred to as the Betz limit, is equal to 0.593, or 59.3% (Nielsen, 2024). This is the point where air begins to pile up if there are no losses other than a reduction in wind speed. The power coefficient, C_p, quantifies the power extracted by wind turbines. The power extracted by a wind turbine, P_{wt} can then be expressed as (Nielsen, 2024):

$$P_{wt} = \frac{1}{2}C_p \rho A_r U^3. \tag{2.21}$$

This thesis focuses on the IEA 15MW offshore reference wind turbine Gaertner et al. (2020b) with the VoltunrUS-S reference semisubmersible platform Allen et al. (2020). The IEA 15MW wind turbine has an C_p of 0.47 at maximum (Gaertner et al., 2020b). The power in the wind, Betz limit and the power extracted by the IEA 15MW wind turbine are illustrated in figure 2.4. Table 2.1 shows some key parameters about the IEA 15MW wind turbine.

2.3.1 Floating wind turbines

Floating wind turbines open up new areas for utilising wind energy, but also present additional challenges. The floating aspect introduces several extra degrees of freedom and the need for a floating substructure. There are four main types of substructures: semi-submersible, spar, tension leg platform, and barge (Nielsen, 2024). This thesis deals with the semi-submersible substructure consisting of 3 vertical columns in a formation around the tower (120-degree angle between each column). Each column has an ordinary catenary mooring line anchored to the seabed.

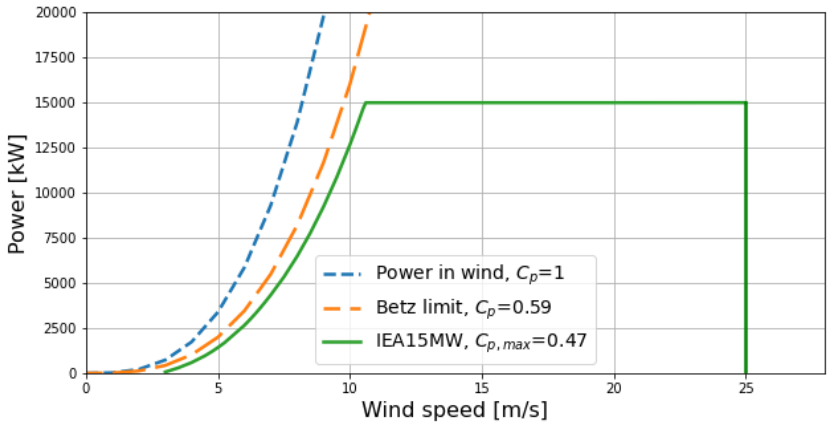

Figure 2.4: Power in wind, Betz limit and the power extracted by the IEA 15MW wind turbine. The power is based on the area of the rotor.

2.3.2 Levelized Cost of Electricity - LCOE

To ensure maximum profitability and return on invested capital, it is crucial to minimise the Levelized Cost of Electricity (LCOE). LCOE is calculated by dividing total costs by total energy produced and is commonly used to compare energy projects Nielsen (2024).

$$LCOE = \frac{Investments + Operational cost}{Energy production} = \frac{I_0 + \sum_{k=1}^{N} \frac{A_k}{(1+i_r)^k}}{\sum_{k=1}^{N} \frac{M_k}{(1+i_r)^k}}, \quad (2.22)$$

where I_0 is the initial investment in year zero, N is the expected lifetime, k is the year of operation, A_k is the operational cost in year k, M_k is the energy produced in year k and i_r is the discount rate that are used in present calculations (Nielsen, 2024). The report by International Renewable Energy Agency (2023) presents the costs of power generation for renewable power. Onshore wind has experienced a 69% reduction in the LCOE from USD 0.107/kWh in 2010 to USD 0.033/kWh in 2022 on a global scale. The LCOE for offshore wind (bottom fixed and floating combined) has decreased by 59% from USD 0.197/kWh in 2010 to USD 0.081/kWh in 2022 on a global scale. This is attributable to a reduction in installation costs and an increase in power generation.

Table 2.1: Parameters of the IEA 15 MW turbine (Gaertner et al., 2020b)

Parameter	Units	Value
Power rating	MW	15
Specific rating	W/m^2	332
Rotor orientation	-	Upwind
Number of blades	-	3
Cut-in wind speed	m/s	3
Rated wind speed	m/s	10.59
Cut-out wind speed	m/s	25
Maximum tip speed	m/s	95
Design tip-speed ratio	-	9 0
Minimum rotor speed	rpm	5.0
Maximum rotor speed	rpm	7.56
Rotor diameter	m	240
Hub height	m	150
Hub diameter	m	7.94
Hub overhang	m	11.35
Rotor nacelle assembly mass	t	1,017
Tower mass	t	860
Blade mass	t	65
Drivetrain	-	Direct drive
Control	-	Variable speed

2.4 Aerodynamics

The design of a wind turbine, particularly its blades, is based on aerodynamic calculations. These calculations are used to determine the aerodynamic loads, which are of significant interest. This thesis will only consider the aerodynamics of the HAWT.

2.4.1 Blade Element Momentum theory

Blade Element Momentum (BEM) theory is a well-established and commonly used method for calculating the aerodynamics of a wind turbine blade. BEM is an extension of the actuator disc theory and consists of two different

theories: blade element theory and momentum theory (Moriarty & Hansen, 2005).
Blade element theory divides the blade into small independent elements. The aerodynamic forces on each element are calculated using the local flow conditions. The total force along the blade is the sum of each element's forces and moments (Moriarty & Hansen, 2005).
Momentum theory, derived from actuator disc theory, states that the pressure (momentum) loss in the rotor plane is caused by the work done on the blade elements by the airflow passing through the rotor plane. These two theories combined lead to each blade element rotating and tracing out circular regions where the momentum theory takes place (Moriarty & Hansen, 2005).

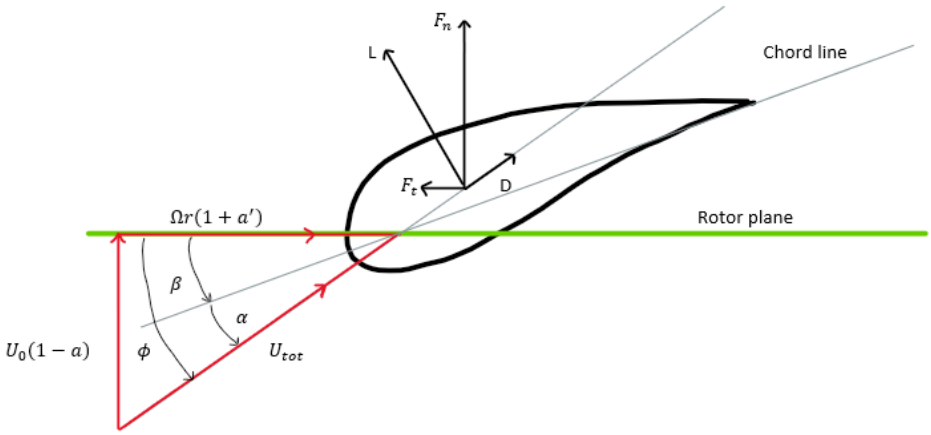

Figure 2.5: 2D blade element with relative wind (U_{tot}) and aerodynamic forces. Figure inspired by (Nielsen, 2024).

The axial induction factor a and the tangential induction factor a' are used to describe how the wind velocity changes are relative to the blade. The axial wind velocity is given by $U_0(1-a)$, where U_0 is the ambient (true) wind. The tangential wind velocity due to rotation is given by $\Omega r(1+a')$. Where Ω is the angular velocity of the rotor and r is the radius of the blade element considered. The axial induction factor is used to express the thrust coefficient that is given by: $C_t = 4a(1-a)$ and the power coefficient $C_p = 4a(1-a)^2$. The momentum loss through the rotor can then be expressed by Bernoulli's equation assuming an incompressible, homogeneous and horizontal flow:

$$F_{loss} = \frac{1}{2}\rho A_{rotor} U_0^2 4a(1-a) \tag{2.23}$$

In figure 2.5 of a 2D blade section the induction factors are represented. The angle of attack, α is the angle between the incoming wind and the chord line. The combination of the twist of the blade section and the pitch angle is denoted β and the angle between the incoming wind and the rotor plane is denoted ϕ and is given by (Nielsen, 2024):

$$\phi = arctan\left(\frac{U_0(1-a)}{\Omega r(1+a')}\right) = arctan\left(\frac{1-a}{\lambda_r(1+a')}\right), \tag{2.24}$$

where $\lambda_r = \Omega r/U_0$ is the local speed ratio. The lift, L, and drag, D, acting perpendicular to and along the incoming wind direction, can be decomposed to find the axial force, F_n, and the tangential force, F_t. The forces can be calculated by (Nielsen, 2024):

$$L = \frac{1}{2}C_l \rho U_{tot}^2 c, \tag{2.25}$$

$$D = \frac{1}{2}C_d \rho U_{tot}^2 c, \tag{2.26}$$

$$F_n = L\cos\phi + D\sin\phi, \tag{2.27}$$

$$F_t = L\sin\phi - D\cos\phi, \tag{2.28}$$

where C_l and C_d are the two-dimensional lift and drag coefficients for the airfoil that depend on the angle of attack and are found by experiments. c is the length of the chord (Nielsen, 2024). By inserting L and D into F_n and F_t and introducing the width of the blade element, dr, the thrust and torque contribution from each element are given by:

$$dT = \frac{1}{2}\rho U_{tot}^2 c(C_l\cos\phi + C_d\sin\phi)dr. \tag{2.29}$$

$$dQ = \frac{1}{2}\rho U_{tot}^2 c(C_l\sin\phi - C_d\cos\phi)dr. \tag{2.30}$$

Blade element theory has limitations. It must account for the loss from induced velocities due to tip vortices, called Prandtl's-loss. As the axial

induction factor increases, the relative wind speed decreases, which reduces the angle of attack. This results in a reduction of lift and drag near the tip (Moriarty & Hansen, 2005). Another limitation of the BEM is that it is invalid for axial induction factors larger than 0.4. This leads to inaccuracies in predicting rotor performance in the turbulent wake state, which occurs at high tip speed ratios, i.e. high rotational speed at low wind speeds (Moriarty & Hansen, 2005). Glauert (1926) addressed this problem and made a correction (Glauert correction) to the rotor thrust coefficient based on experimental data from helicopter rotors. The correction was developed for the entire rotor but is applied at each blade element in BEM. Therefore, it is essential to apply the Glauert correction in conjunction with the tip-loss model to maintain numerical stability and accurate performance assessment of individual blade elements (Moriarty & Hansen, 2005).

2.5 Structural dynamics

Structural dynamics refers to the movement of a structure. The dynamics of a structure are based on Newton's second law (of dynamic equilibrium), which states that the volume of a solid body accelerates due to volume and surface load (Voutsinas, 2010). Floating wind turbines are complex non-linear constructions that undergo a significant amount of loads during operation. The rigid body has six Degrees Of Freedom (DOF), three translational (surge, sway, heave) and three rotational (roll, pitch, yaw), one for each axis. The blades and the tower of a wind turbine are considered flexible beams. These have additional elastic DOF that is related to the deflection and rotation along the span of the components. The elastic DOF is influenced by material properties such as density, stiffness, and damping (Voutsinas, 2010).

2.5.1 Hydrodynamics

Floating wind turbines address new challenges related to the hydrodynamics. The forces of waves, wind, the inertia of the surrounding fluid, the effects of mooring and the hydrostatic forces lead to the equation of motion for a six DOF structure (Nielsen, 2024):

$$(M+A)\ddot{\eta}+(B_v+B_r)\dot{\eta}+(C_m+C_h)\eta=F_{wa}+F_{wi}+F_{cu}+F_{wt}, \quad (2.31)$$

Table 2.2: Natural frequencies and period for different degrees of freedom on the IEA 15MW wind turbine with semi-submersible floater (Gaertner et al., 2020b; Allen et al., 2020).

Degree of Freedom	Natural Frequency [Hz]	Natural period [s]
Surge	0.007	142.9
Sway	0.007	142.9
Heave	0.049	20.4
Roll	0.036	27.8
Pitch	0.036	27.8
Yaw	0.011	90.9
Tower Fore-Aft	0.496	2.0
Tower Side-side	0.483	2.1
Blade Out-of-plane	0.642	1.6
Blade In-plane	0.555	1.8

where η is the six DOF vector where dot and double dot denote velocity and acceleration. M is the 6×6 mass matrix of the wind turbine, A is the hydrodynamic mass matrix, and B_r is the radiation part of the damping matrix that is related to wave generation. B_v is the viscous-related part of the damping matrix. The restoring matrix C_h and C_m are respectively hydrostatic and mooring-restoring. The force vectors denote the excitation forces from water (wa), wind (wi), current (cu) and the forces due to the action of the wind turbine (wi). The damping from the control system should also be considered in either the damping matrix or as a force (Nielsen, 2024).

2.5.2 Morison's equation

The Morison equation is a fundamental equation used in offshore engineering to estimate the wave forces acting on vertical structures such as offshore platforms, piles or offshore wind turbines. It was developed by M. G. Morison in the 1950s and has since become a widely accepted method of predicting these forces. The equation expresses the total force exerted on a structure as the sum of two components: F = F_D (drag force) + F_A (added mass force). The 2-dimensional force on the cylinder also known as the Morison equation is given by (Nielsen, 2024):

$$F_{2D} = \frac{1}{2}\rho C_d D U_{rel}|U_{rel}| + (1 + C_m)\rho\pi\frac{D^2}{2}\dot{U}_{rel}, \tag{2.32}$$

where C_d is the drag coefficient, C_m is the added mass coefficient, D is the diameter of the cylinder, U_{rel} is the relative velocity between the fluid (wave, current and motion of the floater) and the cylinder, and $\dot{U}_{rel}$ is the acceleration of the fluid (Nielsen, 2024).

2.5.3 Structural loads

As wind turbines increase in size and power capacity, the impact of structural loads caused by aerodynamic and gravitational forces becomes more apparent. If left unaddressed, these loads can adversely affect the performance of the turbine and potentially lead to premature failure of the system. Therefore, it is crucial to comprehend the complex relationship between structural loads, and power generation, as well as their impact on the turbine's lifespan.

Structural loads in a three-bladed wind turbine are primarily caused by aerodynamic imbalances in the rotor and blades. There are two primary occurrences of loads to consider. 1P and 3P loads, named according to their frequency. 1P loads, also known as 'once per revolution', occur with a frequency equal to the rotor speed. These imbalances are caused by fluctuating wind profiles and vertical wind shear, resulting in asymmetrical loads across the rotor disk (Niebsch et al., 2010). Since aerodynamic imbalances occur once per rotor revolution, mitigating the 1P loads is important (Njiri & Söffker, 2016). The 1P loads are highly connected to the fatigue damage discussed in the next section. 3P (3 times 1P) loads are related to the blade passing frequency and are mainly caused by tower shadow effects as the blade passes the tower and wind shear (Bhattacharya, 2019). As seen in figure 2.6 the 1P and 3P frequencies are not two single frequencies, but a frequency band corresponding to the operational range of the rotor. In addition, the structural load of the turbine is affected by gyroscopic effects caused by rotor rotation, blade pitching, and nacelle yawing (Njiri & Söffker, 2016). In the design phase, it is crucial to consider frequency to prevent resonances between external loads and the natural frequencies of the wind turbine (Gaertner et al., 2020b).

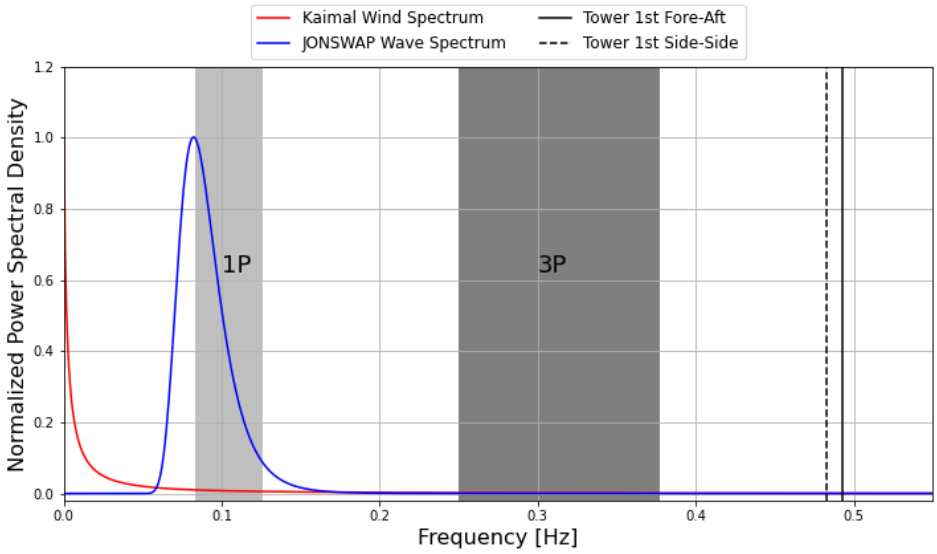

Figure 2.6: Frequency spectrum. Inspired by (Allen et al., 2020)

A detailed analysis of the structural loads at the main components of a wind turbine is of significant interest, with a particular focus on the shear forces and moments experienced in the blade root, tower top and tower base regions. Figure 2.7 illustrates the structural loads in the spanwise and streamwise directions. Spanwise is along the rotor plane of the turbine and is also referred to as the ”in-plane” or ”side-side” direction. In contrast, the streamwise direction is perpendicular to the rotor plane and faces the wind. Streamwise direction is also referred to as the ”out-of-plane” and ”fore-aft” direction. An understanding of these forces and moments is essential for evaluating the structural integrity and performance of the wind turbine under various operating conditions and environmental factors.

2.5.4 Damage equivalent load

The components of a wind turbine are designed to withstand the momentary loads that may occur during operation. However, they must also be able to withstand fatigue loads. Fatigue is the change in material properties (damage and failure) caused by cyclic loading (Suresh, 1998). The total damage is the sum of the damage fractions contributed by each load case i in the time series, and can be calculated by Palmgren-Miner’s rule (Freebury & Musial,

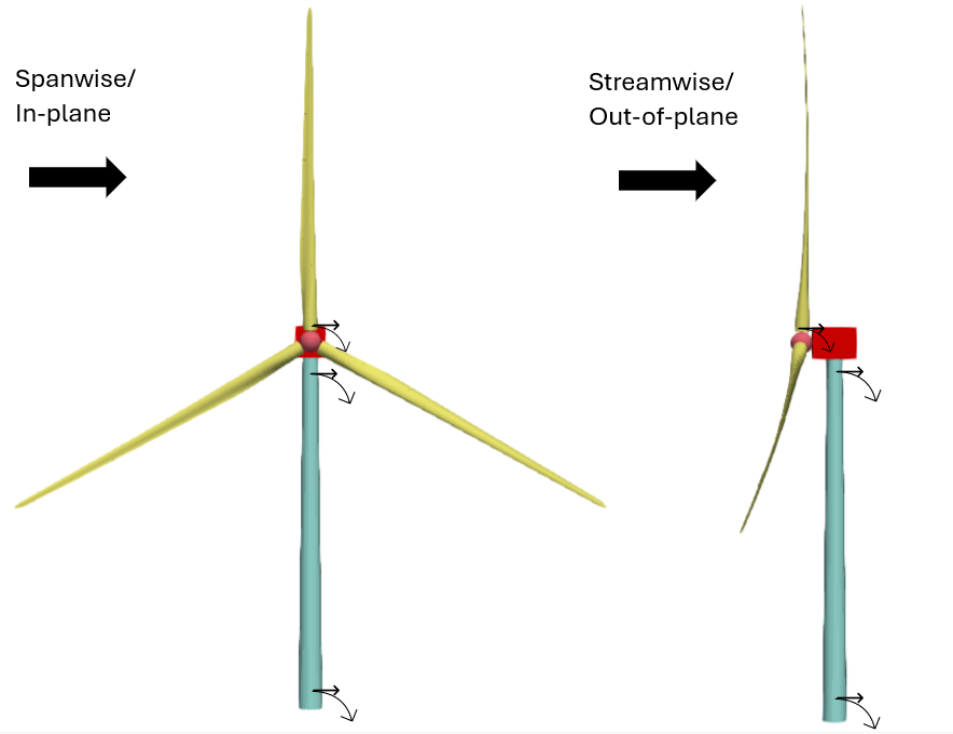

Figure 2.7: Structural loads: Spanwise and streamwise shear forces (straight arrows) and bending moments (curved arrows) at the blade root, tower top and tower base.

2000):

$$Damage = \sum_{i}^{j} \frac{n_i}{N_i}, \tag{2.33}$$

where i is the load case number, j is the total number of load cases, n_i is the number of load cases for each case i, and N_i is the number of load cycles to failure for case i (Freebury & Musial, 2000). The load cycles on wind turbine components are often stochastic and have variable amplitude, which must be accounted for when calculating fatigue loads. Frandsen & Christensen (1994) developed a method to achieve this by calculating the Damage Equivalent Load (DEL). This accounts for the amplitude of each case i, and the number of oscillations in the time series of loads:

$$DEL = \left[\frac{\sum_i F_i^m n_i}{n_{eq}} \right]^{\frac{1}{m}}, \tag{2.34}$$

where F_i represents the load range for each load cycle, n_i is the number of load cases for each case i, n_{eq} is the number of equivalent cycles and m is the Wöhler exponent which is dependent on the material properties (Frandsen & Christensen, 1994). The number of equivalent cycles is determined using the Rainflow cycle counting algorithm that was developed by Tatsuo Endo and M. Matsuishi in 1968 (Matsuishi & Endo, 1968).

2.6 Wind Turbine Control

This section explains how a wind turbine controller works. A variable-speed wind turbine is a wind turbine that can adjust the rotational speed of the rotor to operate under a wide range of wind speeds. The main operational functions of a variable speed wind turbine controller are (Nielsen, 2024):

- Controlling the generator torque to maintain a desired optimum rotational speed.
- Controlling blade pitch to control power output above rated speed.
- Controlling the yaw angle to ensure the turbine faces the mean wind direction.

To ensure optimum performance and avoid damage, the blade pitch and generator torque control must be fast-acting. The yaw control is not as important. It is therefore controlled so that the wind turbine faces the several-minute average wind direction. The control system also has to manage special events such as start-up and shut-down procedures, and grid failures, and contribute to damping of turbine motions (Nielsen, 2024). Figure 2.8 illustrates the various control regions that are present in a wind turbine. Regions 1 and 4 are situated outside the operational wind speeds, and no power generation occurs in these regions. Region 2 represents the operational region between the cut-in and rated wind speeds. In this region, the wind turbine operates with a variable rotor speed to extract the maximum possible power from the wind. This region is controlled by the generator torque,

which adjusts the torque according to the rotational speed of the rotor. Region 3 is the region between the rated and cut-out wind speeds. The wind speed is too high to extract maximum power, and the turbine is at its rated power. In this region, the generator torque is either constant or aims to hold a constant power output. The rotational speed of the rotor is held constant by a pitch controller, which pitches the blades to adjust the angle of attack. Region 2.5 is the region at rated wind speed, situated between regions 2 and 3. In this region, the transition from torque control to pitch control occurs.

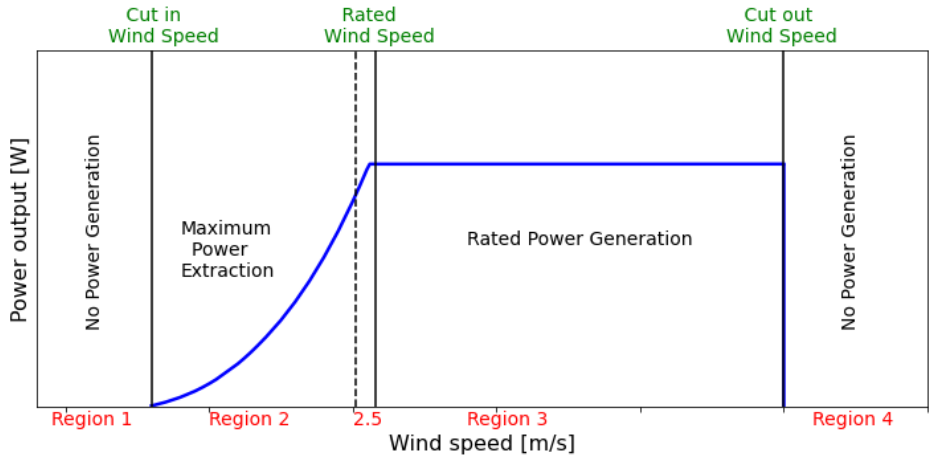

Figure 2.8: Control regions compared to a typical variable-speed wind turbine power-curve.

2.6.1 PI controller

The most common way to adjust the generator torque and blade pitch angle during operation is by a reference tracking Proportional-Integral (PI) controller. The PI controller determines how much and quickly correction is applied by using varying amounts of proportional and integral action on the input signal. In the time domain, the PI controller is given as (Abbas et al., 2022):

$$y(t) = K_p u + K_i \int_0^t u dt \tag{2.35}$$

where u is the input signal and y is the output signal from the controller. K_p and K_i are respectively proportional and integral gains. The input and output vary depending on the operational region of the wind turbine. Under rated wind speed the wind turbine is controlled by reference tracking generator torque control. Then the input and output are given by (Abbas et al., 2022):

$$u = -\Delta\omega_g, y = \Delta\tau_g. \tag{2.36}$$

In the above-rated operational region, the input to the controller is the same, but the output is made to adjust the blade pitch.

$$u = -\Delta\omega_g, y = \Delta\beta, \tag{2.37}$$

where $-\Delta\omega_g = \omega_{g,ref} - \omega_g(t)$, $\Delta\beta$ and $\Delta\tau_g$ can be expressed the same way (Abbas et al., 2022). For a direct drive wind turbine -$\Delta\omega_g$ is equal to the rotational speed of the rotor $-\Delta\omega_r$.

2.7 Control strategies

Due to the nonlinearity, and the stochastic wind, it is difficult to create a mathematical model that can predict the dynamics of the system (Njiri & Söffker, 2016). The deployment of optimal control strategies is essential for the minimization of structural loads and the optimization of power production Meyers et al. (2022). This study investigates the control strategies included in this section.

2.7.1 Variable speed torque control

The generator torque in a standard variable speed torque control is determined based on the rotational speed of the rotor. Figure 2.9 shows a typical torque schedule relative to the rotational speed. Region 1 is the start-up region where the rotor accelerates to the minimum operational rotor speed. In region 1.5, the generator torque increases relatively fast with wind speed to slow down the acceleration of the rotor and start the power extraction.

Region 2 which is the primary operational region for the torque controller, the generator torque (τ_g) is regulated by this expression (Johnson, 2004):

$$\tau_g = K\omega^2, \tag{2.38}$$

where K is a constant proportional gain, and ω is the rotational speed of the rotor. K is determined to maximise the power and is found by the C_p curve of the wind turbine. There is no accurate method for determining the constant gain. The wind speed varies spatially, forcing the turbine to operate suboptimally, even if an accurate approximation is assumed, either numerically or experimentally (Johnson, 2004). Region 2.5 is the transition region between torque control and pitch control and the torque increases with wind speed to avoid too high rotor speed. In Region 3, the aim is either constant power or constant generator torque. The pitch control is responsible for regulating the speed of the rotor. For FOWT the constant generator power is often replaced by constant generator torque to improve platform stability (Gaertner et al., 2020a).

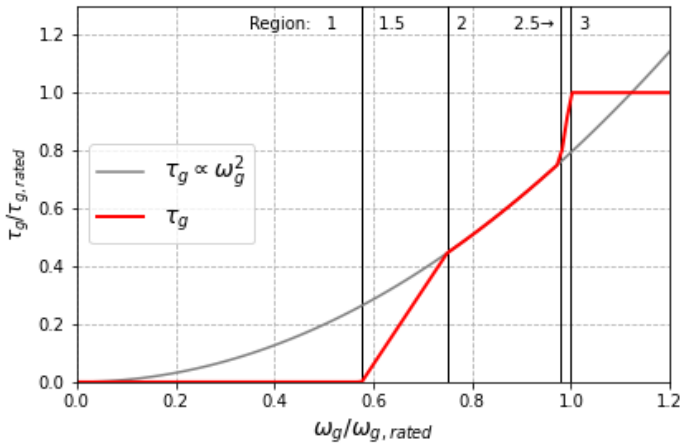

Figure 2.9: Standard generator torque control schedule relative to rotor speed. Figure inspired by (Pöschke & Schulte, 2021).

2.7.2 Tip Speed Ratio tracking torque control

Tip Speed Ratio (TSR), denoted by λ, is the relationship between the speed of the blade tip and the wind speed and is given by (Ragheb, 2014):

$$\lambda = \frac{\text{tip speed of blade}}{\text{wind speed}} = \frac{\omega R}{U} \tag{2.39}$$

where ω is the rotational speed of the rotor in rad per second, R is the radius in meters and U is the relative wind speed between the blade tip and the free wind velocity when taking surge and pitch motion into account. This is the most common control strategy below-rated wind speed to extract as much as possible power from the wind. The TSR holds significant importance in the designing of a wind turbine. The power coefficient C_p is closely related to the TSR. Each wind turbine has an optimum TSR for maximum power extraction, which depends on the number of blades and rotor blade design. As wind speed fluctuates, the control system must adjust rotor speed by torque control and pitch the blades to maintain TSR at its optimal value, see figure 2.10. Too high TSR can produce increased aerodynamic loads on the blades. This is caused by the turbulent wake left by the blade. The next blade that follows will hit the turbulent wake from the previous blade. Too low TSR during low wind speed leads to power loss due to insufficient extraction of energy in the wind due to the wind that passes in between the blades (Ragheb, 2014). When the TSR tracing controller is active, the value of K in equation (2.38) is dependent on the TSR and is given by (Johnson, 2004):

$$K = \frac{1}{2}\rho\pi R^5 \frac{C_{p,max}(\beta,\lambda)}{\lambda^3}, \tag{2.40}$$

where λ is the optimal TSR corresponding to the maximum power coefficient. The TSR tracking control presents some challenges as it depends on the incoming wind, which is difficult to measure (Johnson, 2004). The large rotor inertia also prevents the rotor from adapting to the rapid changes in wind speed (Bossanyi, 2003a).

2.7.3 Pitch saturation/Peak shaving

Peak shaving is a technique used to reduce high peaks in rotor thrust. The highest peaks in the thrust force occur near the rated wind speed of the wind turbine. To reduce the thrust, the pitch controller is saturated to pitch

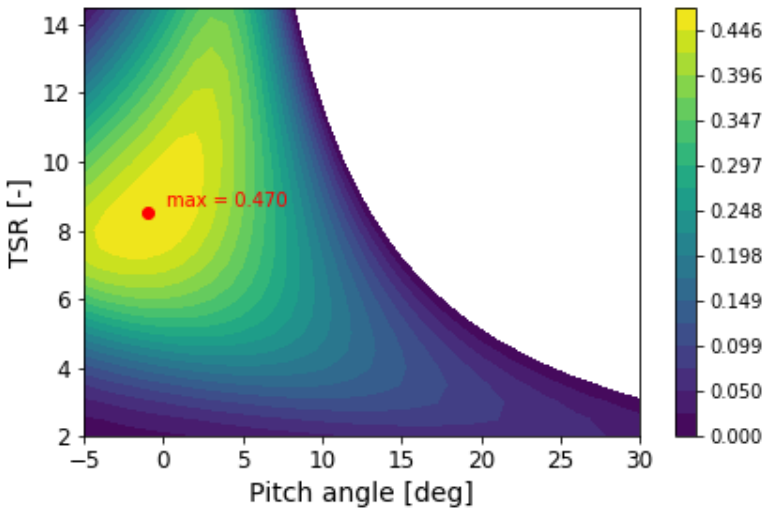

Figure 2.10: TSR-Pitch-Cp relation in the IEA 15MW wind turbine. Made with ROSCO toolbox (NREL, 2021).

the blades to a minimum angle of $\beta_{min}(U)$, as a function of wind speed. This ensures that the peak is shaved, see figure 2.11. Reducing the rotor thrust force results in lower tower base loads (Abbas et al., 2021). As the pitch saturation results in a minimum pitch schedule (minimum pitch to a given wind speed), the turbine will operate at a higher pitch than necessary, reducing efficiency near the rated wind speed. The control system designer must optimise the tradeoff between power and reduced loads to ensure the wind turbine operates sustainably (Abbas et al., 2021). The IEA 15MW wind turbine has a minimum rotation speed to avoid resonances. This implies that the turbine operates at a higher rotational speed than the optimal tip speed ratio would suggest. In this situation, it is possible to use pitch saturation to maximise power production at low wind speeds. To extract as much energy from the wind as possible, a minimum pitch schedule is set while the torque control ensures a minimum rotation speed (Abbas et al., 2021). This can be seen in figure 2.11 at lower wind speeds.

2.7.4 Individual Pitch Control

The most common method for pitching the blades of a wind turbine is through Collective Pitch Control (CPC). As the name suggests, the blades

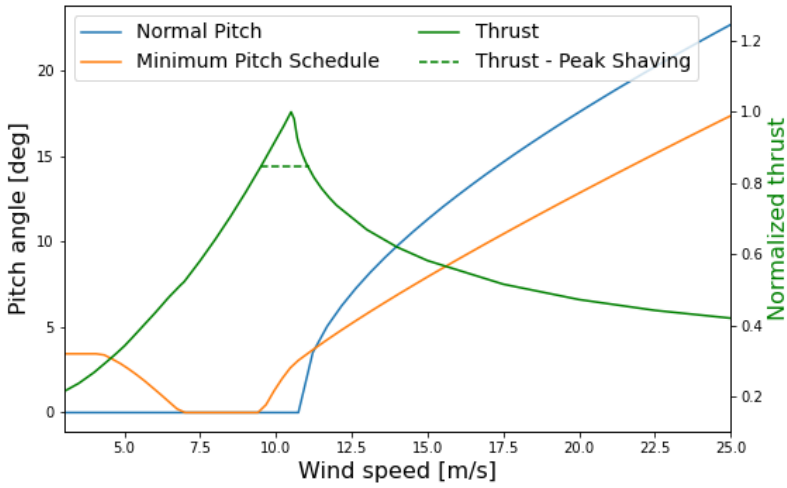

Figure 2.11: Pitch schedule and normalized thrust for the IEA 15MW wind turbine with and without pitch saturation (peak shaving). Made with ROSCO toolbox (NREL, 2021).

are collectively pitched simultaneously and with the same amount of pitch. Individual pitch control allows for dynamic and independent pitching of each blade. IPC has been implemented to reduce asymmetric structural loads caused by aerodynamic imbalances, (i.e., 1P loads) (Tang et al., 2021). Typical IPC implementations use blade-root-based load sensing to provide feedback to the IPC algorithms. There are some additional costs associated with IPC due to the cost of the sensors themselves, the cost of installation/maintenance of the sensors and the additional pitch activity required.

2.7.5 Active power control/Constant power in control region 3

The constant power control strategy is an alternative to the constant generator torque controller in control region 3. Unlike the constant torque controller, the constant power controller does not aim to hold the generator torque constant. Instead, it aims to hold the power output constant and uses the rated power as a reference. It then regulates the generator torque inversely proportional to fluctuations in rotor speed to mitigate the fluctuations that arise from the wind (Aho et al., 2012). It is often beneficial for a turbine to

maintain a constant power output to facilitate an optimal interaction with the electricity grid. To maintain a constant frequency, the grid must balance the power generated and consumed, as well as account for grid losses (Aho et al., 2012). This is more easily achieved when the power from a wind turbine is held constant, as fluctuations in power output can be less pronounced. As wind turbines will account for an increasing proportion of electricity generation on the grid, this will become increasingly important (Aho et al., 2012).

2.8 Controller Methodology in IEA 15MW FOWT

The IEA 15MW wind turbine is controlled by two active proportional-integral (PI) controllers for generator torque and blade pitch angle. The minimum speed of 5 rpm is set to avoid 3P interference with the tower's natural frequency. The rated speed is 7.55 rpm at 10.59 m/s, giving a maximum rated tip speed of 95 m/s, resulting in an optimum TSR of 9 (Gaertner et al., 2020a). The operation of the control system is divided into three main regions, with additional sub-regions in between the main regions. The main regions are (Gaertner et al., 2020a):

- 3 m/s $\leq U \leq$ 6.98 m/s: minimum rotor speed. A TSR tracking PI controller on the generator torque regulates the minimum rotor speed at 5 rpm. In this region, the TSR is too high (more than 9) due to the minimum rotational speed of the rotor and low wind speeds. The pitch angle is in this region determined using a look-up table based on the filtered hub-height wind speed to optimise the power coefficient.
- 6.98 m/s$\leq U \leq$ 10.59 m/s: optimal TSR. At below-rated wind speeds, the rotor speed is controlled to operate at the turbine's optimum TSR using a PI controller on the generator torque.
- 10.59 m/s $\leq U \leq$ 25 m/s: rated power. Above-rated wind speeds, the main goal is to maintain the rated rotor speed value at 7.55 rpm. This is done by a PI controller on the blade pitch angle.

This chapter has now presented the background theory on which the method and results are based.

Chapter 3

Methods

This chapter describes the research design, how the LLJ and waves are generated, the modelling tools used for simulation, and the configurations of the controller.

3.1 Research design

Five different controller configurations have been studied in this thesis. This was done in combination with different cases, each representing an LLJ with a different core-wind speed and height. The cases were constructed using the IEA 15MW wind turbine power curve, hub height and observations of LLJs. The study by Wagner et al. (2019) revealed that the average low-level jet core height was 236 metres and the average core speed was 11.8 metres per second over the Southern North Sea. The real low-level jets (cases 4 and 8) were constructed by the observed low-level jets in Bakhoday-Paskyabi et al. (2022). This study aimed to investigate the fully active control system and selected cases based on control region 2.5 (at rated wind speed) and control region 3 (above rated wind speed). The control strategies peak shaving and individual pitch control have been developed for these control regions respectively. It is also in these regions that wind turbines experience the greatest loads, and therefore, load mitigation has the greatest potential. This study examines the structural shear forces and moments experienced at both the top and base of the tower, as well as the structural shear force and moments acting at the blade root. This is based on previously conducted studies by Ahmed (2023) and (Gutierrez et al., 2017). An illustration of the

location of the loads can be found in figure 2.7.

3.1.1 Cases

Eight wind cases have been chosen. Cases 1−4 are in control region 2.5, and cases 5−8 are in control region 3. The four controller groups designated A, B, C and D, will hereafter be referred to by the names displayed under ”Name” in table 3.2. Each wind case is simulated for each controller group, 1A, 1B, 1C, 1D, 2A, 2B etc. In case 5−8 controller group B is exchanged with B(2). Each simulation lasted 720 seconds, with the first 120 seconds removed to eliminate the model's spin-up period.

Table 3.1: Wind cases.

Wind case	LLJ type	Wind speed [m/s]	LLJ core height [m]
1	Ideal	11.5	90
2	Ideal	11.5	150
3	Ideal	11.5	210
4	Real	11.5	230
5	Ideal	17	90
6	Ideal	17	150
7	Ideal	17	210
8	Real	17	270

Table 3.2: Controller groups.

Control group	Name	Controller setting
A	Default	CPC + TSR-tracking torque control
B	CT	TSR-tracking turned OFF
C	PS	Pitch Saturation turned ON
D	IPC	IPC turned ON
B(2)	CP	Constant power (region 3)

The Default controller is a standard TSR tracking torque controller with a collective blade pitch controller. The default uses the TSR tracking torque

control in control region 2.5 and constant torque control above in region 3. The other control strategies are variants of Default. CT (changing torque) is a variant of Default where TSR tracking is turned off. This is a controller that changes the generator torque proportional to the square of the rotor speed (see section 2.7.1 and equation 2.38) This control strategy was chosen based on tests that demonstrated differences in the rotational speed of the rotor during an LLJ when TSR tracking torque was turned off. The estimation of wind speed is a crucial aspect of TSR tracing torque control, particularly in the case of a 240-meter vertical LLJ wind profile, which presents certain challenges in achieving an accurate estimation of wind speed. PS and IPC refer to peak shaving and individual pitch respectively, and were chosen based on previous studies. In control region 3, case 5-8 the CT is exchanged with (CP) constant power, denoted B(2) in the table. This exchange was made because CT also employs constant torque control above rated wind speed (control region 3) and would not differ from the Default in this control region. More information on the controller settings is provided in section 3.2.3.

3.1.2 Generating low-level jets

This thesis's ideal low-level jet generation was based on the paper Zhang et al. (2019), which established an engineering LLJ inflow model. The model consists of the average wind field and the fluctuating wind field, where the average wind field part is used in this thesis. The average wind field is based on the theory of plane wall jets in fluid mechanics. This theory creates a free jet velocity profile, therefore the expression where modified to satisfy the no-slip condition at the ground. The LLJ velocity was then given as (Zhang et al., 2019):

$$v_{LLJ}(z) = \left\{ v_{ref} + v_m \left[1 - \tanh^2 \left(C_s \frac{z - z_s}{z_s} \right) \right] \right\} \left(\frac{z}{z_{ref}} \right)^a, \qquad (3.1)$$

where z is the height, z_s is the height of maximum velocity of the jet, z_{ref} is the reference height, v_{ref} is a reference velocity, v_m is the jet velocity, C_s is a shape parameter and a is the shear exponent (Zhang et al., 2019). The LLJ velocity equation (3.1) was used to generate the LLJ wind profiles listed in table 3.1.

3.1.3 Generating waves - JONSWAP spectrum

The waves are modelled by Hydrodyn, a submodule in Openfast. Hydrodyn employs the JONSWAP spectrum to model the waves and requires the significant wave height (H_s) and the wave period (T_p) to create the wave model. For a fully developed sea, H_s and T_p can be calculated as functions of the 10-meter mean wind speed. These are calculated in accordance with the methodology outlined in the study by Ahmed (2023) and the paper by Ahmed & Paskyabi (2023), and are given by (Carter, 1982):

$$H_s = 0.0248 U_{10}^2, \tag{3.2}$$

$$T_p = 0.729 U_{10}, \tag{3.3}$$

where U_{10} is the mean wind speed at 10 meters. The H_s and T_p values are calculated for each case individually.

3.1.4 Calculation of Damage Equivalent Loads

The damage equivalent loads were calculated in accordance with the methodology employed in the aforementioned study by Ahmed (2023). The Python algorithm used, developed by Ahmed can be found in this source: Ahmed (2024). The Wöhler exponent m was set to 10 for the blade root (composite) and 3 for the tower (steel).

3.2 Modelling tools

This section provides an overview of the modelling tools and the setup used in this thesis.

3.2.1 Generate turbulence - TurbSim v2.0

The LLJ velocity profiles generated and listed in table 3.1 were given as input to TurbSim to generate turbulence boxes. In TurbSim, the wind was generated using the Kaimal spectrum, and the coherence was modelled using the Davenport model. The decay coefficients were calculated by (Cheynet et al., 2018):

$$c_1^u = 11.0 + 1.8\exp(4.5\zeta) \tag{3.4}$$
$$c_1^v = 7.1 + 3.4\exp(6.8\zeta) \tag{3.5}$$
$$c_1^w = 3.5 + 0.7\exp(2.5\zeta), \tag{3.6}$$

where ζ is the stability parameter that is calculated by the formula:

$$\zeta = \frac{z}{L}, \tag{3.7}$$

where z is the reference height and L is the Obukhov length. Based on the observational data of an LLJ in Bakhoday-Paskyabi et al. (2022) the reference height was 15 meters, with an Obukhov length of 250 meters. This results in a $\zeta = 0.06$. The turbulence intensity under the same conditions was 8%. The roughness length was kept constant at 0.001 for all cases.

Table 3.3: TurbSim input

Parameters	Settings
Turbulence model	ICEKAI
Turbulence intensity [%]	8
Roughness length [m]	0.001
c_1^u	13.4
c_1^v	12.2
c_1^w	4.3

3.2.2 Wind turbine response - OpenFAST v3.5.0

The turbulent boxes created in TurbSim were used as an input to OpenFAST to generate the turbine response. OpenFAST is an open-source software supported by the National Renewable Energy Laboratory (NREL). The software is a multiphysics, multi-fidelity tool consisting of sub-modules. It couples nonlinear aerodynamics, hydrodynamics, control systems and structural dynamics simulations in the time domain (Jonkman et al., 2005). The relevant sub-modules used in this thesis are described below:

InflowWind provides wind conditions for aerodynamic and structural simulations. In this study, InflowWind utilises the binary wind field generated by TurbSim as an input and passes it to OpenFAST. InflowWind is also capable of utilising other types of binary wind fields and inbuilt wind fields, including uniform wind with shear profiles and steady winds (NREL, 2023).

AeroDyn is responsible for the aero-elastic simulation and the aerodynamic calculations on the blades and the tower. AeroDyn incorporates blade geometry, airfoil characteristics, and the impact of incoming wind in its calculations, employing BEM theory to determine the aerodynamic forces acting on the blades (NREL, 2023).

HydroDyn is a sub-module provided for offshore turbines, including both bottom-fixed and floating structures. It considers the effect of currents and waves on the structure. The software program HydroDyn enables users to employ a variety of techniques for calculating the hydrodynamic loads on a structure. These include strip theory and potential flow theory (NREL, 2023). In this thesis, HydroDyn utilizes the JONSWAP wave spectrum to simulate irregular waves and uses Morison's equation to calculate wave loads.

Elastodyn is responsible for modelling the structural dynamics of the wind turbine, including loads, deflection and movements. The submodule calculates the distribution of loads and moments among the various components of the wind turbine, taking into account the properties of the material. The values generated by Elastodyn correspond to nodes distributed throughout the wind turbine structures. ElastoDyn incorporates nonlinear effects such as material damping and stiffness variation (NREL, 2023).

Servodyn is the control system module. It encompasses a range of control settings and strategies, including generator control, blade pitch, yawing, start-up and shut-down (NREL, 2023). This module can be connected to other controllers via a Bladed-style DLL (in this study ROSCO) to enable further user-defined functionality. A schematic block diagram of Openfast and the connection between the submodules are shown in figure 3.1.

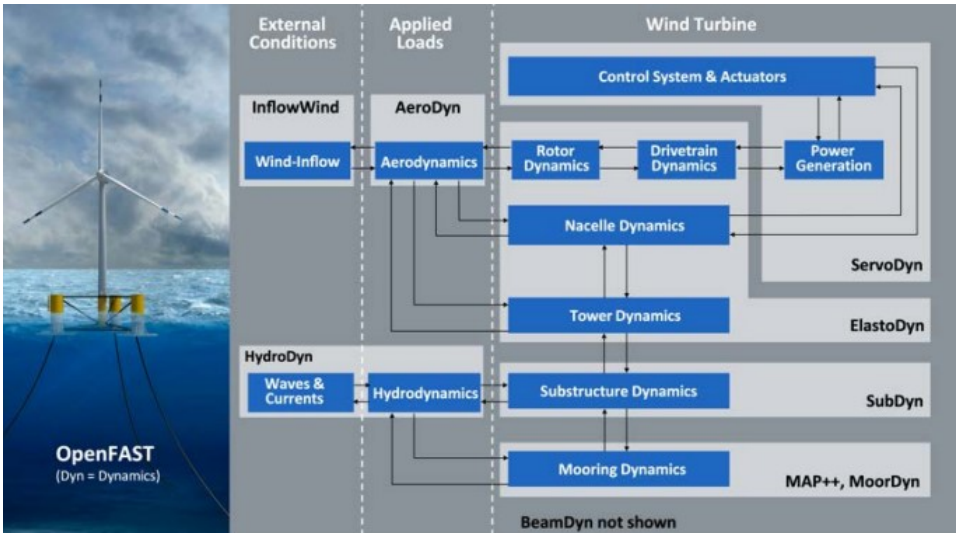

Figure 3.1: Openfast submodules interaction. Adapted from NREL, (Ross et al., 2022).

3.2.3 Controller configuration - ROSCO v2.7

ROSCO is a Reference Open-Source Controller for fixed and floating offshore wind turbines, developed by researchers at the Delft University of Technology (Abbas et al., 2021). It follows standard industry practices and facilitates controller tuning. Its primary function is to maximize power in below-rated wind speeds and regulate rotor speed in above-rated operations (Abbas et al., 2021).

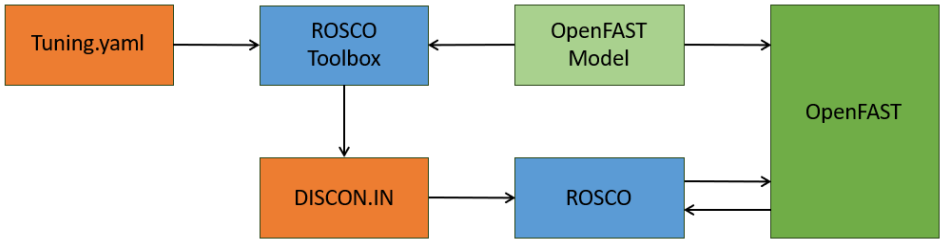

Figure 3.2: ROSCO workflow and connection to OpenFAST. Inspired by (Abbas et al., 2021).

Figure 3.2 shows the ROSCO workflow and its elements. ROSCO consists of two parts: the ROSCO toolbox and ROSCO. Setting up the controller

using the ROSCO toolbox involves utilising the Tuning.yaml file and the OpenFAST Model to establish and fine-tune the controller. ROSCO toolbox runs a code called CCBlade to generate a rotor performance table (C_p surface). CCBlade is a blade momentum solver from WISDEM that predicts the aerodynamic loading of wind turbine blades using the BEM theory (Ning, 2013). ROSCO Toolbox utilises the rotor performance table to optimise the PI gains for the torque and pitch controller. ROSCO requires the control parameters omega and zeta, which respectively correspond to the controller's desired natural frequency and desired damping ratio (Abbas et al., 2021). Additionally, the DISCON.IN file gets written through this process. The DISCON.IN file contains the controller gain schedule and a set of various controller flags that can be switched on and off in the DISCON.IN file without the need to rerun the ROSCO toolbox (Abbas et al., 2021). The controller setup used in this thesis is shown in table 3.4.

Table 3.4: Default controller setup in DISCON.IN file. The first three controller flags are edited for each simulation (alternative simulation setting in parentheses), while the last six are constant. Any additional controller flags not listed are unused.

Controller Flags	Setting	Functionalities
VS-ControlMode	2 (0)(1)	2: TSR tracking below rated, constant torque above rated 0: square law below rated 1: constant power above rated
IPC-ControlMode	0 (1)	0: off 1: 1P reductions
PS-Mode	0 (1)	0: no pitch saturation 1: implement pitch saturation
SS-Mode	1	1: introduce setpoint smoothing
PC-ControlMode	1	1: active PI blade pitch control
WE-Mode	2	2: Extended Kalman Filter
Fl-Mode	2	2: feed back rotational veloicty
F-NotchType	2	2: tower-top fore-aft motion
F-LPFType	2	2: second-order low-pass filter

Dynamic linked library

When OpenFAST is running, the ROSCO controller utilizes the data from DISCON.IN and interacts with OpenFAST through the bladed-style control interface. This interface connects the ROSCO controller to the corresponding DLL (Dynamically Linked Library) and OpenFAST. The external controller, ROSCO, operates in discrete time, communicating on a fixed time step, similar to internal controllers. (DNV, 2024).

Controller logic

Figure 3.3 shows how the controller uses the feedback from the wind turbine as input to make new outputs. The turbine gives the controller $\dot{x}_t$, which is the tower top fore-aft acceleration, τ_g is the generator torque, β is the collective blade pitch angle, and ω_g is the generator speed. These parameters pass by the yellow boxes which are filters, and the orange boxes which are various controller modules, before they are passed to the blue boxes which are the pitch angle and generator torque controller. (Abbas et al., 2022).

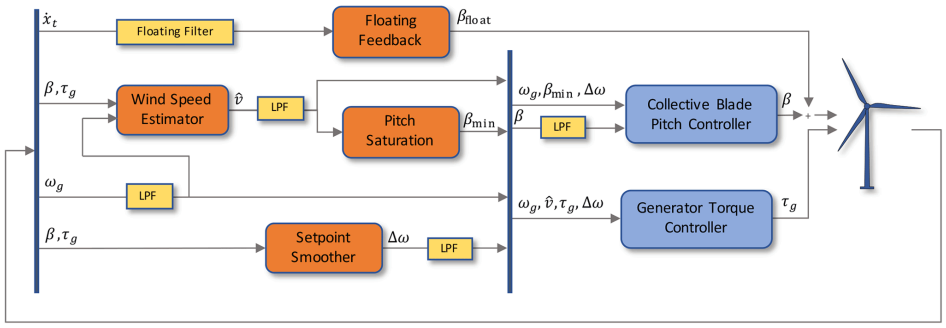

Figure 3.3: Block diagram showing the general ROSCO controller logic. Adapted from (Abbas et al., 2022)

ROSCO must respond quickly to input data to provide feedback to OpenFAST. This is made possible by solving a basic first-order equation that represents the wind turbine:

$$\dot{\omega}_g = \frac{N_g}{J}(\tau_a - N_g \tau_g \eta_{gb}), \tag{3.8}$$

where ω_g is the generator speed, N_g is the gear ratio, J is the rotor inertia, η_{gb} is the generator efficiency, τ_g is the generator toque, and τ_a is the aerodynamic torque that is given by:

$$\tau_a = \frac{1}{2}\rho A_r \frac{C_p(\lambda,\beta)}{\omega_r} v^3, \tag{3.9}$$

where ρ is the air density, A_r is the rotor area, C_p is the power coefficient, ω_r is the rotor speed and v is the wind speed. The power coefficient $C_p(\lambda,\beta)$ value is found in the rotor performance table created by the ROSCO toolbox. The IEA 15MW wind turbine has a direct drive shaft and doesn't utilize any gearbox. This implies that the value of N_g in equation (3.8) is equal to 1 and that the generator speed is equivalent to the rotor speed.

Peak shaving

ROSCO permits the user to select the peak shaving factor. In this study, a nominal peak shaving factor of 0.8 was employed. This implies that ROSCO will limit the thrust to 80% of the maximum, which equates to a 20% reduction in the maximum thrust. The factor of 0.8 leads to the pitch schedule in figure 2.11.

Chapter 4

Results and discussions

This chapter presents and discusses the simulation results. The results are divided into two sections, one for each control region and additional subsections covering aerodynamic loads, structural loads, and power output (electricity generation). Furthermore, a comprehensive discussion is presented. Figure 4.1 shows the eight low-level jet cases that are investigated in this thesis.

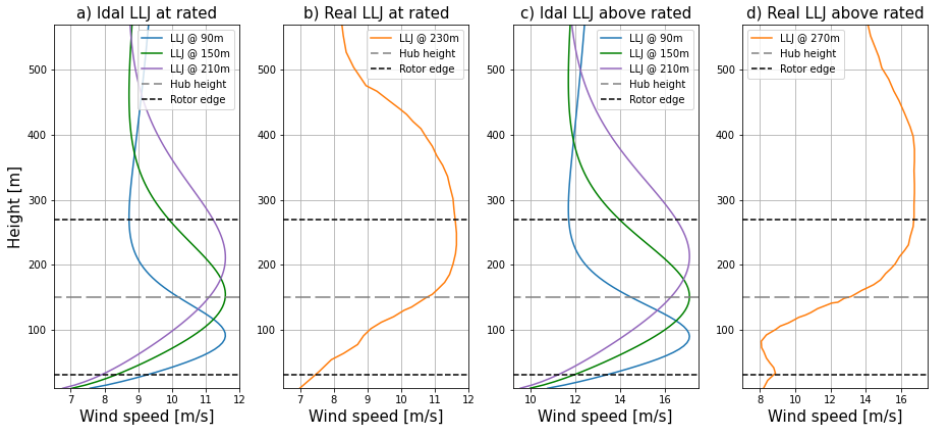

Figure 4.1: LLJ profiles: a) case 1−3, b) case 4, c) case 5−7, and d) case 8.

To provide an initial visualization of the performance of the control strategies, a 100-second time series of case 1 is presented in figure 4.2. The time series illustrates the response of pitch angle, rotor thrust angle, and generator power to wind fluctuations. The control strategies provide different pitch angles, which affect the turbine's response. IPC and PS have

distinct pitch schemes, oscillating and steady high respectively, as shown in the figure.

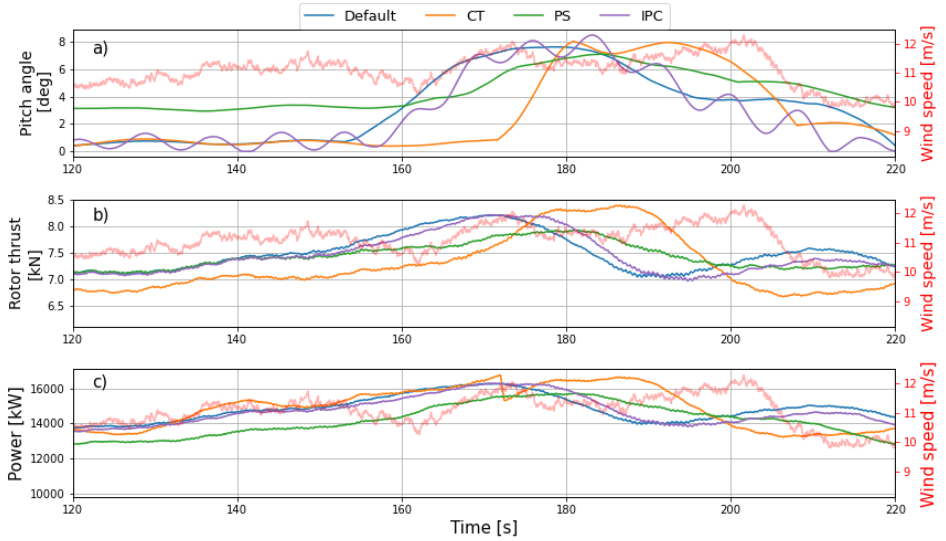

Figure 4.2: A 100-second time series of case 1 that shows: a) blade 1 pitch angle, b) rotor thrust, and c) power output for all controller groups. The wind speed is shown in red in the background.

4.1 At rated wind speed/control region 2.5

In this section, the results of cases 1−4 are presented, which are at rated wind speed and in control region 2.5.

4.1.1 Aerodynamic loads

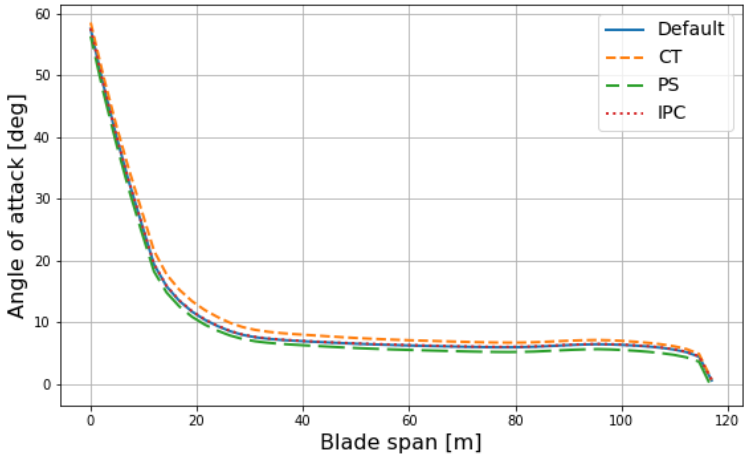

Figure 4.3: Mean local angle of attack along the blade for case 1.

Figure 4.3 shows the local angle of attack along the blade for case 1, which also represents the trend for cases 2−4. The blade is designed to have the highest twist angle (16 degrees) at the blade root with a decreasing twist towards the tip with a minimum of −2.5 degrees 100 meters from the blade root. The twist results in a more consistent angle of attack along the blade, as the tangential wind speed is higher towards the tip. The chord length is also longest near the root of the blade and becomes smaller towards the tip. The combination of twist angle and chord length results in a more uniform distribution of the aerodynamic forces along the blade. Figure 4.4 shows the local mean thrust and torque along the blade span in cases 1−4. At low pitch angles at rated wind speed, the angle of attack is positive along the whole length of the blade, which leads to high thrust and torque at the outer part of the blade. A higher pitch scheme in PS results in a significantly lower mean thrust and torque along the blade in all cases. An increase in pitch (clockwise rotation of the blade in a clockwise rotating turbine) results in a reduction in the angle of attack, which in turn leads to a decrease in thrust. The lifting force is reduced and the torque thereby decreases. Another significant difference is the high torque that occurs with CT. Compared to default, CT has a lower rotor speed which on average varies from 94% to 96% relative to default. The reduced rotational speed leads to a reduced tangential wind speed and an increased angle of attack as seen in figure 4.3. The thrust shows less variation with CT; in case 1, it is slightly lower, while

in case 3, it is higher than default.

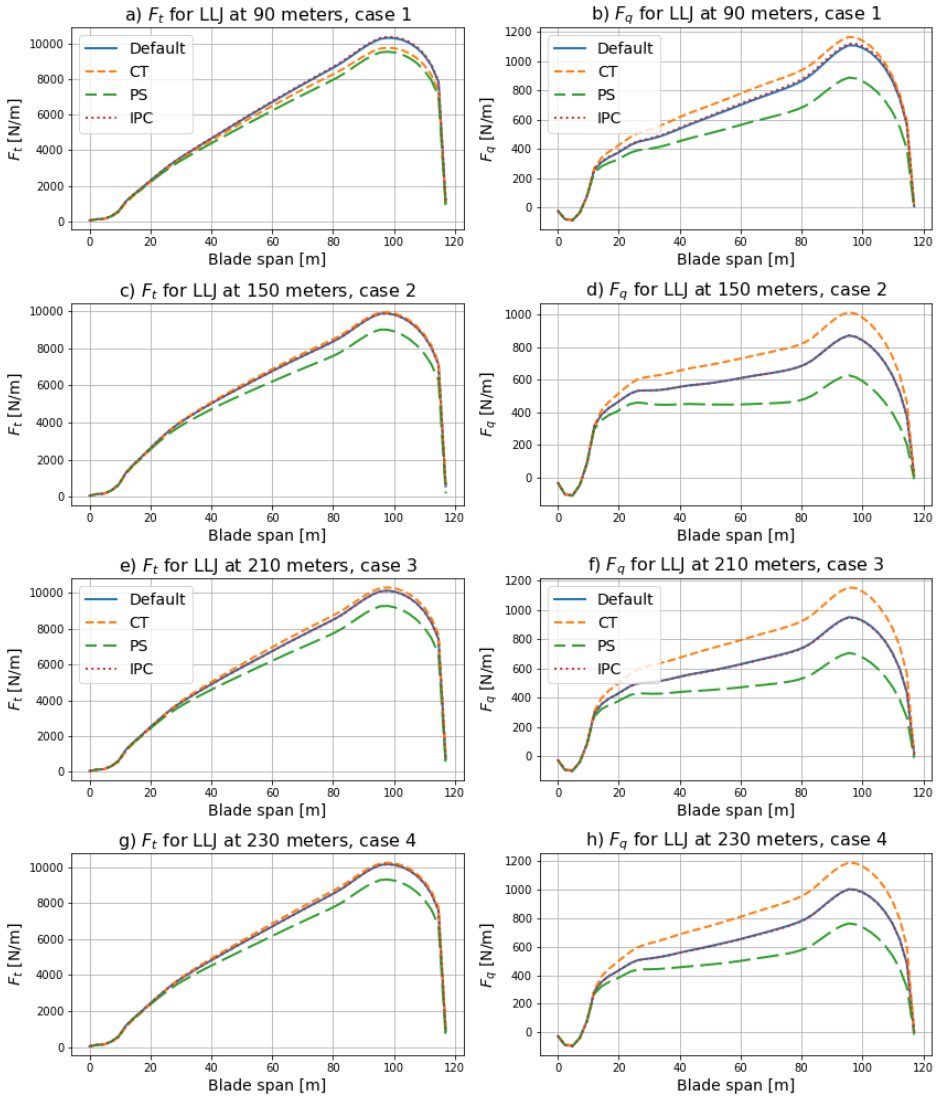

Figure 4.4: Local mean thrust, F_t and torque F_q along the blade for case $1-4$.

There is little to no difference in the average aerodynamic loads between IPC and default. However, some differences are better shown in the time series of the total thrust and torque along the blade. These characteristics are demonstrated in figure 4.5 and 4.6. Between $160-190$ seconds in Case 1, it is shown that the IPC has smoother thrust variations with lower amplitude

in the oscillation than the default. This is due to the individual pitch, which results in a more consistent angle of attack when the wind speed is different above and below the hub. It is also possible to notice these slightly smaller amplitudes with IPC in the other cases, except for case 2. In case 2, the LLJ core is at the height of the hub and the IPC does not offer any advantage in terms of aerodynamic forces. This is likely due to the symmetry in wind speed above and below the hub.

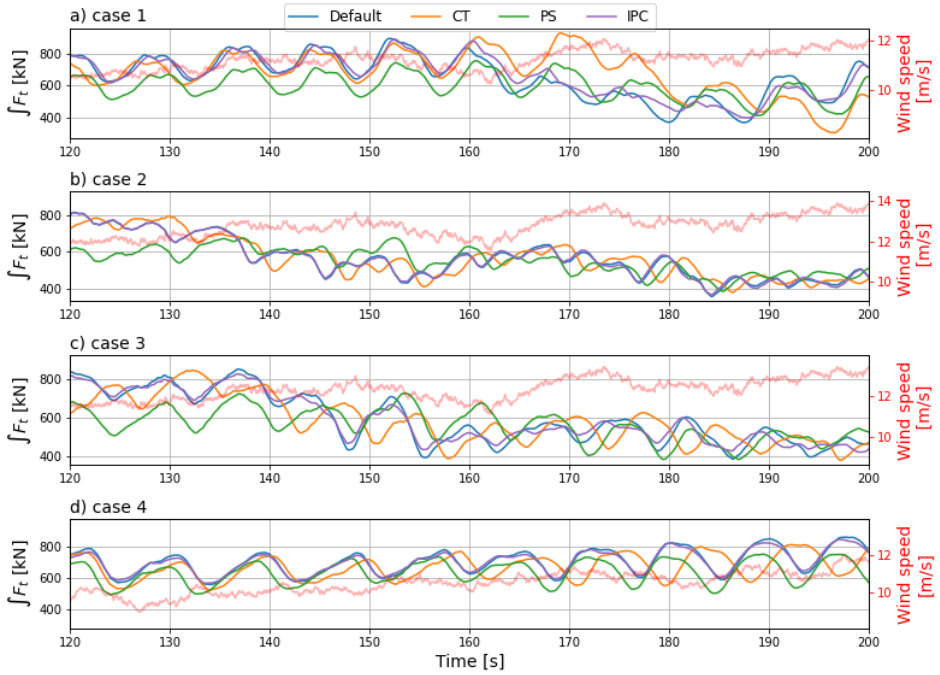

Figure 4.5: Time series of the integrated (total) thrust force along the blade.

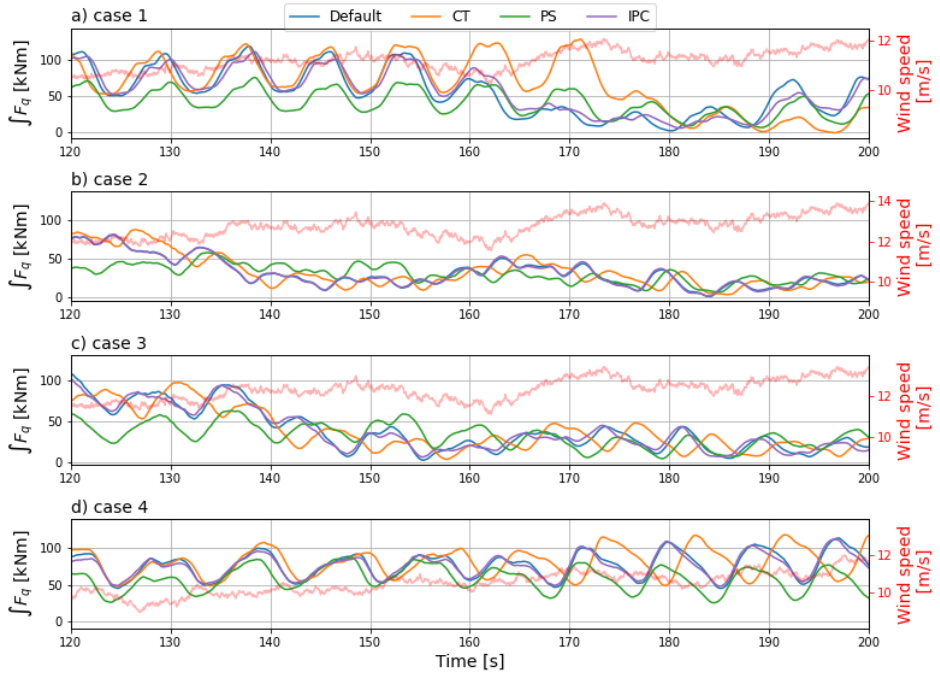

Figure 4.6: Time series of the integrated (total) torque along the blade

Figure 4.7 illustrates the maximum total thrust and torque normalized relative to the default controller. The greatest reduction is observed in PS, which results in an $11-16\%$ reduction in maximum thrust and a $12-26\%$ reduction in maximum torque compared to default. IPC does not lead to any particular change in maximum thrust, less than 1% compared to default. The CT exhibited a fluctuating trend, with an increase in thrust ranging from 2 to 4% in cases 1, 3, and 4, and a reduction of less than 1% in case 2 compared to default. Conversely, the torque exhibited a $6-15\%$ increase across all cases with CT compared to default.

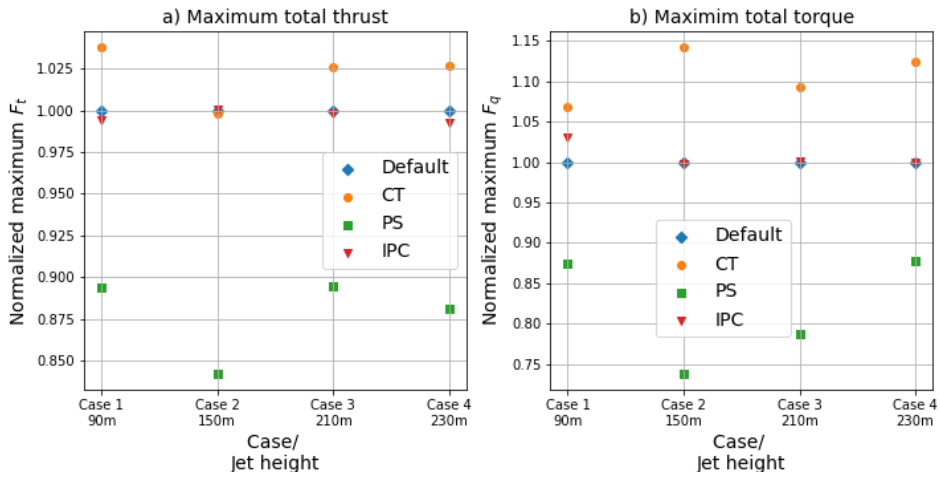

Figure 4.7: Normalized maximum total thrust and torque compared to the default controller for case 1−4.

4.1.2 Structural loads

This section presents the structural loads at the base of the tower, the top of the tower, and the root of the blade for cases 1−4. The load is expressed as damage equivalent load.

Tower base

Figure 4.8 shows the damage equivalent loads on the tower's base. Figure 4.8a and b shows that PS significantly reduces streamwise shear force and bending moment, with minimal variation across the cases compared to the other control strategies. The reduction in streamwise shear force and moment is likely attributable to the substantial reduction in thrust observed in PS. The other control strategies exhibit considerable variability across the cases, with varying LLJ heights. It can be observed that the implementation of IPC does not result in a significant difference in the streamwise loads, but does differ from the default in the spanwise tower base loads. In Case 1, when the low-level jet height is at 90m, the implementation of IPC reduces the damage equivalent loads by 32 and 40% in spanwise shear and moment, respectively compared to the default. In case 2 and 3, the spanwise loads are equal to the default value. However, in case 4, the introduction of IPC results in a significant increase in the spanwise loads compared to default.

These differences are likely due to the presence of a large negative shear in case 1 and a strong positive shear in case 4. In the streamwise direction, CT exhibited a variety of outcomes, while in the spanwise direction, the damage equivalent loads were found to be equal to the default value in case 1, but significantly larger in the other cases. This discrepancy can be attributed to the high torque due to the slightly lower rotational speed in CT compared to default.

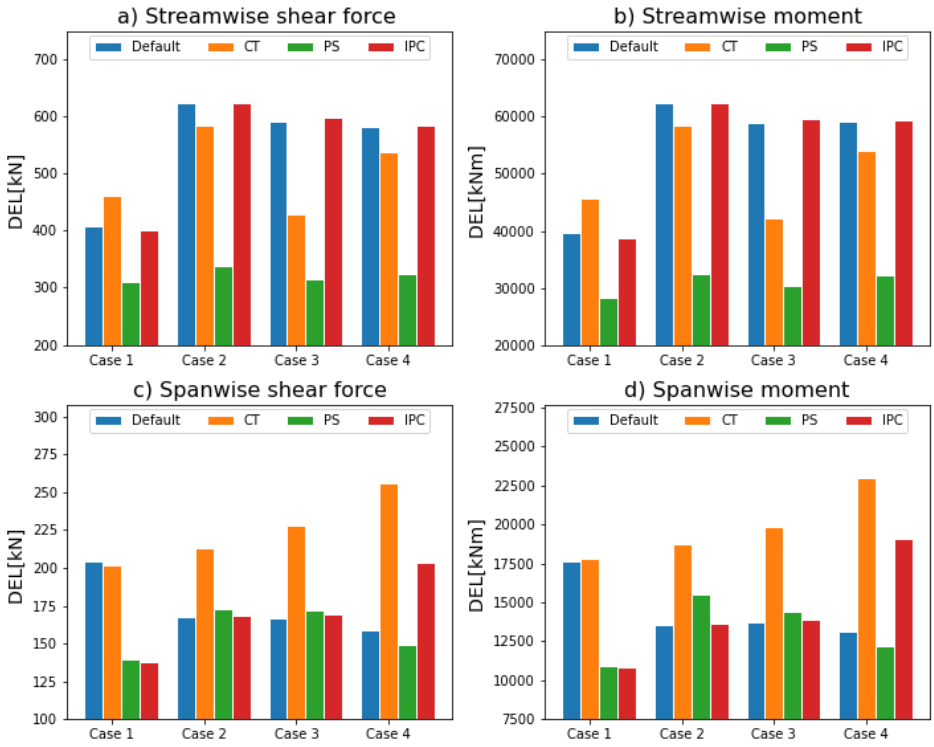

Figure 4.8: Damage equivalent load at the base of the tower for case 1−4.

Tower top

Figure 4.9 shows the damage equivalent loads at the top of the tower. IPC doesn't provide any improvements in the streamwise direction and has the same pattern in the spanwise loads as at the tower base. The results of the PS indicate a reduction and consistent streamwise shear force across all cases, although the other loads vary. In case 1, the spanwise loads in PS are reduced,

while in the other cases, the values are approximately equal to the default. The CT configuration exhibits a higher damage equivalent streamwise shear load in case 1, in comparison to the other cases. The streamwise moment remains consistent with the default configuration, while the spanwise loads are elevated in all cases, except the spanwise shear force in case 1, which is reduced.

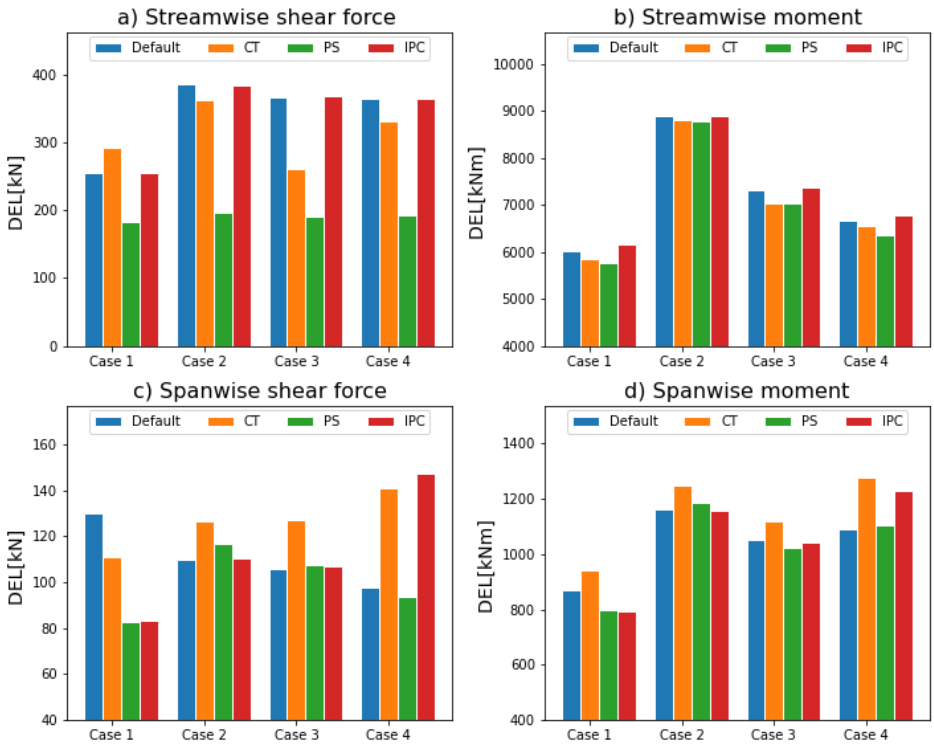

Figure 4.9: Damage equivalent load at the top of the tower for case 1−4.

Blade root

Figure 4.10 shows the damage equivalent loads at the root of the blade. The higher pitch schedule in PS has been demonstrated to reduce the aerodynamic thrust, which is reflected in the out-of-plane shear force and bending moment. PS exhibits significantly lower out-of-plane loads in all cases compared to default. In contrast, the in-plane loads at the blade root are not reduced with PS and are slightly higher than the default in all cases. IPC

reduces the out-of-plane loads, except in case 2, where it is equal to the default. In case 2, the LLJ height is at hub height, resulting in a symmetry in the wind profile above and below the hub. The in-plane loads are not remarkably influenced by IPC and CT. The results of the out-of-plane loads in CT are variable. In cases 1 and 4, the shear force and bending moment results indicate a higher damage equivalent load for CT, while in cases 2 and 3, there is a reduction in load compared to default.

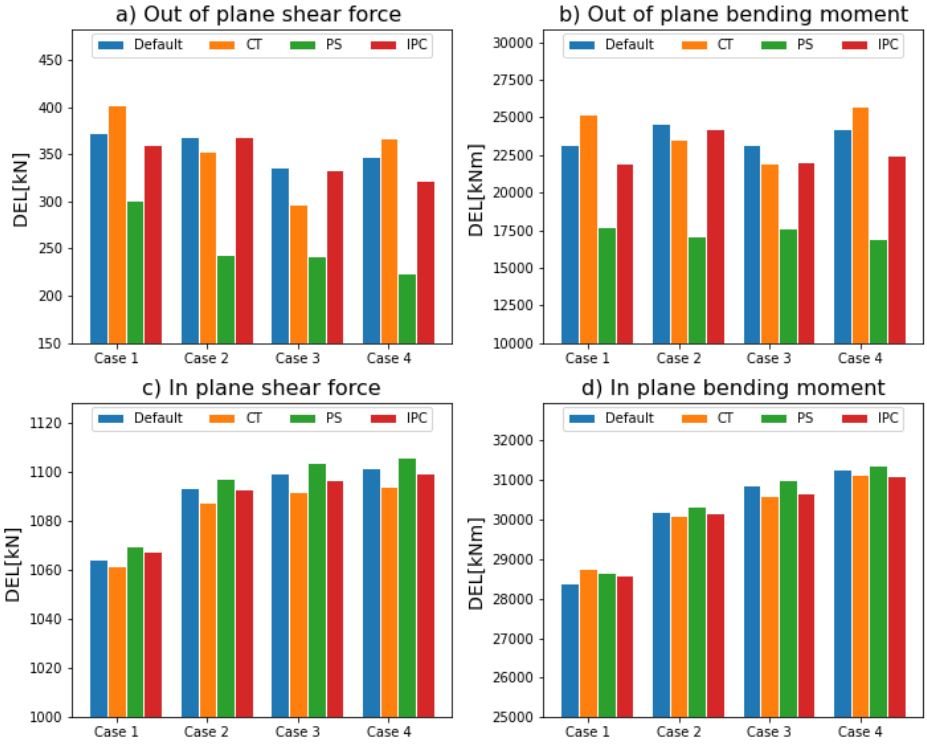

Figure 4.10: Damage equivalent load at the blade root for case 1−4.

4.1.3 Energy production

Figure 4.11 shows how much energy the wind turbine has generated under the 600-second long simulation for each controller strategy in each case. CT is the control strategy that extracts the most power from the wind and generates the most energy in all cases. The biggest difference is in case 3 where CT produces 61 kWh (2.6%) more than the default controller.

This is a significant increase in energy production over 10 minutes. This phenomenon can be attributed to the TSR tracking torque controller in the default configuration, which utilises the filtered wind speed at hub height to provide the optimal TSR. However, this approach is suboptimal in cases where the LLJ wind profile is present, as the wind speed is often higher at hub height and lower towards the tips. The CT allows the rotor speed to determine the generator torque response, which results in a lower rotational speed that is more suitable for the LLJ. The lower power generation observed for PS is consistent with expectations. The higher pitch schedule results in less thrust and torque, which implies that less power is extracted and less energy is generated. The implementation of IPC does not result in any change in energy production compared to the default configuration.

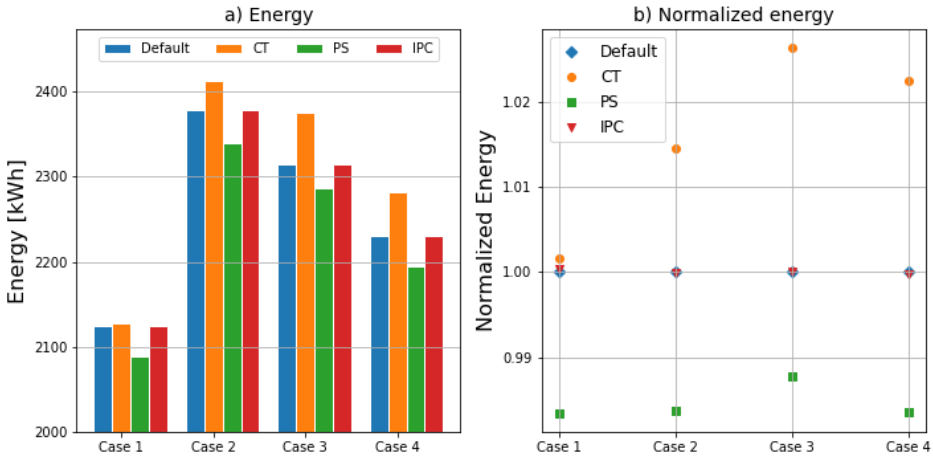

Figure 4.11: Energy produced in 600 seconds for case 1−4.

4.2 Above-rated wind speed/control region 3

In this section, the results of cases 5−8 are presented, which are above-rated wind speeds. Remember that in cases 5−8 the control strategy CT (TSR turned off below rated and constant torque above rated) is replaced with CP (constant power) to distinct from the default controller that also utilizes constant torque in control region 3, above rated wind speed.

4.2.1 Aerodynamic loads

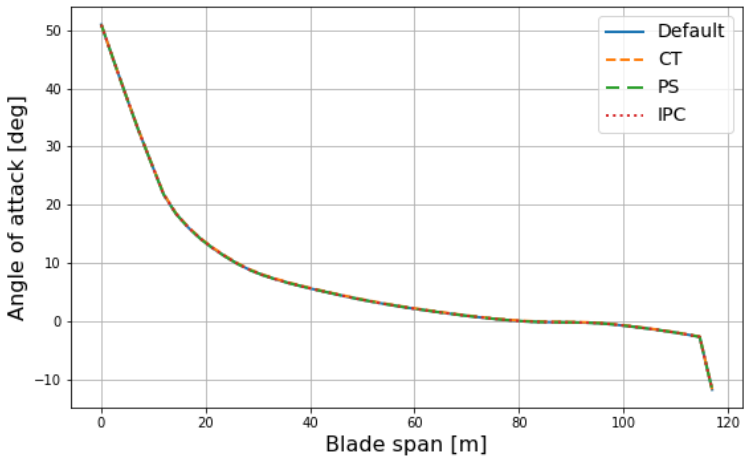

Figure 4.12: Mean local angle of attack along the blade for case 6.

In control region 3, the blades pitch to maintain the rated rotor speed. An increase in pitch results in a reduction in the angle of attack, whereas an increase in wind speed leads to an increase in the angle of attack. To maintain a constant power extraction when the wind is increasing, the blades are pitched to decrease the thrust and to prevent the blades from stalling (loose the lift force). At some point, the pitch can be negative towards the tip of the blade, which implies that the blade does not extract power from the wind and the thrust turns negative. Figure 4.12 of the angle of attack along the blade in case 6 illustrates the phenomenon of negative angles of attack. In all cases within this control region, a negative angle of attack was observed. However, case 6 exhibited the greatest proportion of this phenomenon. This is most likely due to the LLJ height in case 6 being at hub height, which implies that the tip of the blade experiences a lower wind speed than the blade near the hub. Lower wind speed also contributes to a decrease in the angle of attack. The local mean aerodynamic loads along the blade in cases $5-8$ are shown in figure 4.16. There are small to no differences in the local mean thrust forces along the blade for the various control strategies in this region. The maximum thrust occurs around 90 meters from the blade root in cases 5 and 8, which are the ideal LLJ at 90 meters and the real LLJ profile at 270 meters. In cases 6 and 7, the maximum thrust occurs around 35 meters from the blade root, which is most likely due to the height of the

LLJ at 150 and 210 meters. At the blade tip, the thrust is negative due to the negative angle of attack which occurs towards the tip at higher pitch angles. The local mean torque along the blade experiences a maximum of around $25-30$ meters with a sudden increase at the very tip of the blade. The only differences between the control strategies are in case 8 where CP differs with a higher mean torque from 25 meters from the blade root and towards the tip.

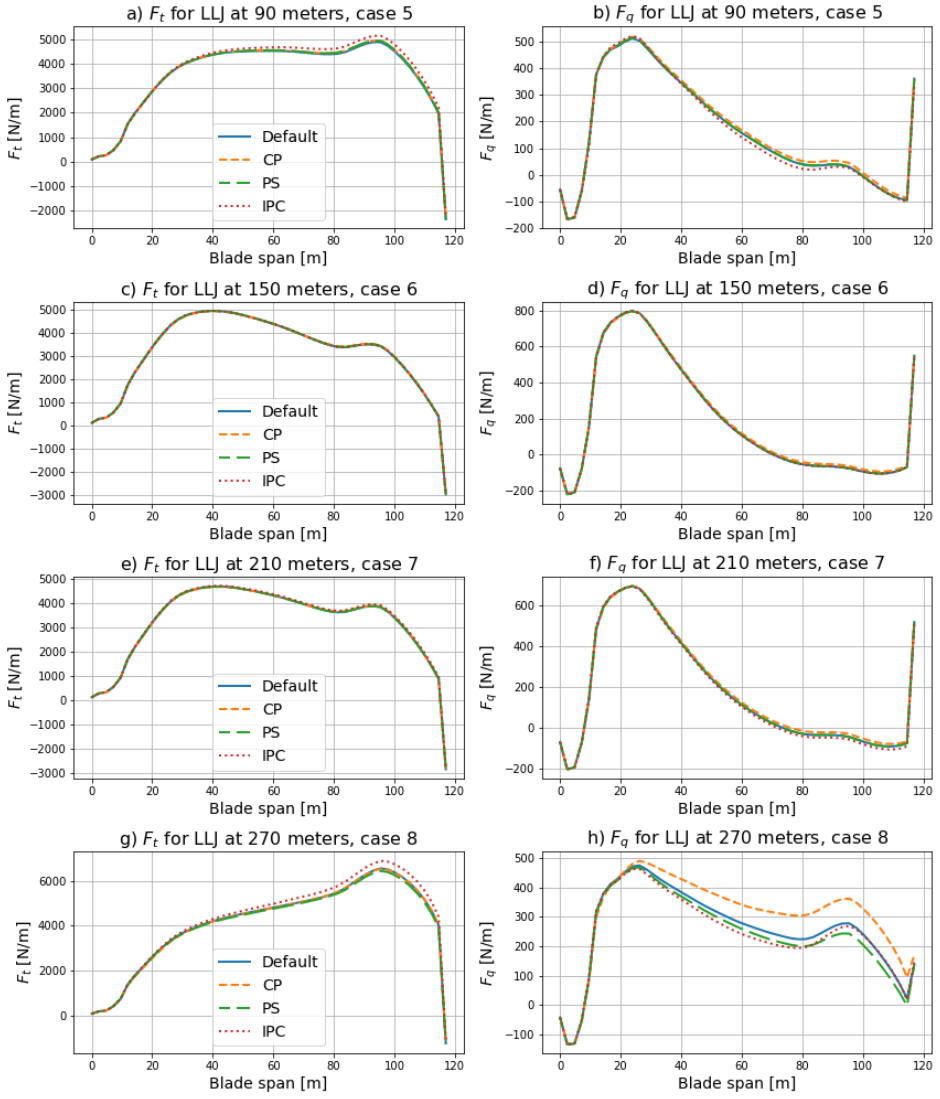

Figure 4.13: Mean thrust, F_t and torque F_q along the blade for case $5-8$.

Figure 4.14 and 4.15 show an 80-second long time series of the total thrust and torque loads (integrated over blade span). This shows that IPC smoothens the amplitude and reduces the oscillations in the thrust and torque during operation. Especially in cases 5 and 7 where the LLJ height is at 90 and 210 meters respectively, IPC reduces the asymmetric loads that the LLJ causes. In case 6 where the LLJ is at hub height, IPC did not lead to any improvements due to the symmetric wind under and above the hub. During the real LLJ profile in case 8, IPC also provided benefits when the wind turbine was subjected to a high positive shear.

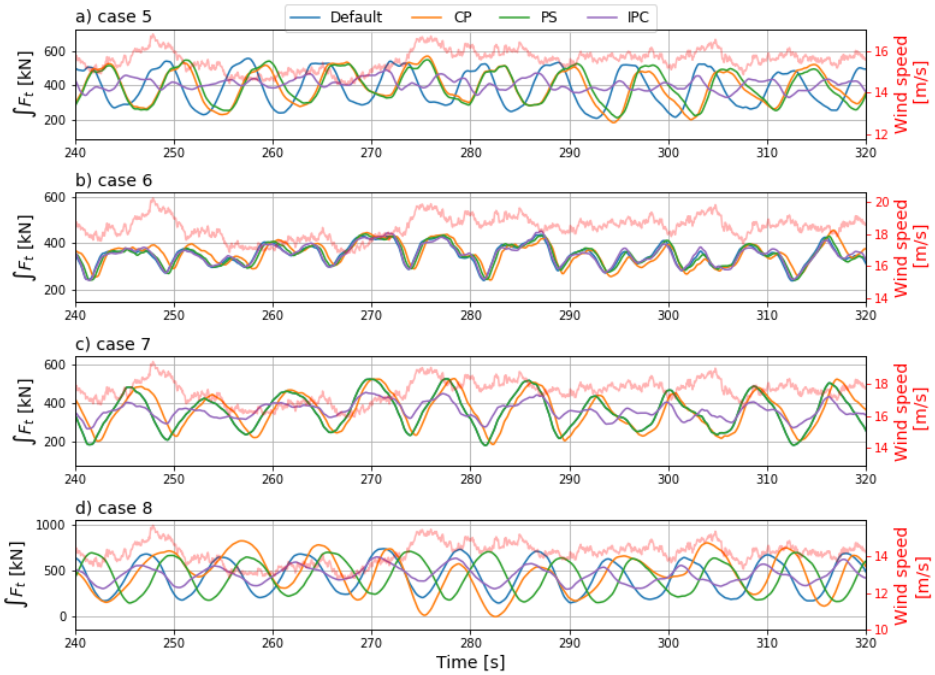

Figure 4.14: Time series of the integrated (total) thrust force along the blade.

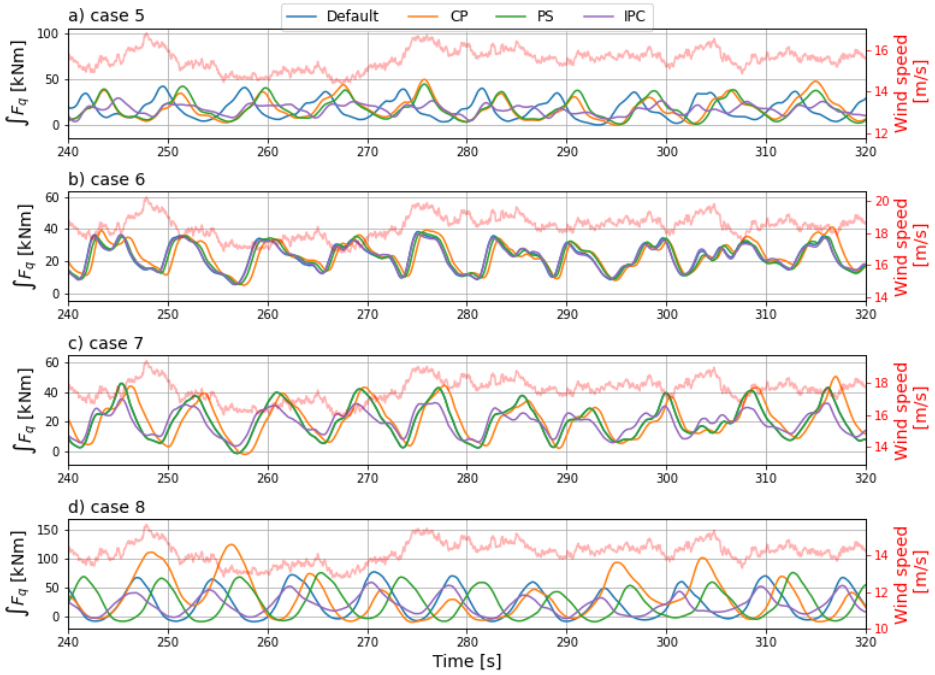

Figure 4.15: Time series of the integrated (total) torque along the blade.

Figure 4.16 shows the maximum total aerodynamic loads that occurred during the simulation. CP which changes the generator torque to maintain a more constant power output experiences both the highest maximum thrust and torque. IPC reduces the maximum aerodynamic loads in all cases except case 6 where the LLJ is at hup height. PS doesn't differ much from the default controller except in case 8. When the LLJ is at 270 metres, the mean vertical wind speed is low due to the high shear, resulting in a lower pitch angle. PS is then activated in a manner that does not pitch to lower angles but rather remains at a higher pitch to reduce the loads.

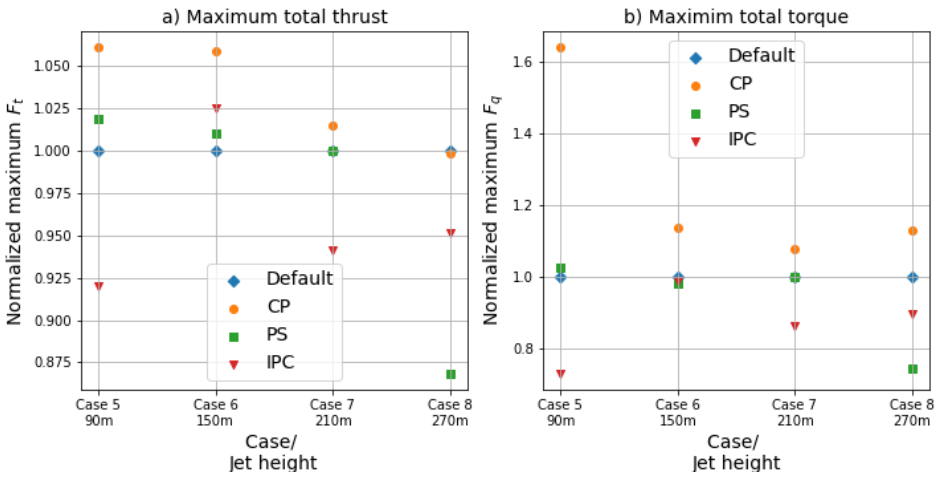

Figure 4.16: Normalized maximum total thrust and torque compared to the default controller for case 5−8.

4.2.2 Structural loads

This section presents the structural loads at the base of the tower, the top of the tower, and the root of the blade for cases 5−8. The load is expressed as damage equivalent load.

Tower base

The damage equivalent structural loads at the tower base are shown in figure 4.17. The utilisation of CP leads to an increase in the streamwise tower base damage equivalent loads compared to default. Additionally, the spanwise loads increase when CP is employed, except for case 1. The elevated loads are likely attributable to the generator torque, which undergoes fluctuations and contributes to greater variations and oscillations than the constant generator torque, which is employed in the default configuration. It can be observed that the implementation of IPC does not result in any reduction in load at the tower base compared to default. However, IPC does lead to an increase in all loads in case 8 and the spanwise moment in case 5. In contrast, PS is observed to result in a significant reduction in the spanwise loads in case 5, with an LLJ at 90 metres, compared to the default. Furthermore, in case 8, the streamwise loads are mitigated by PS.

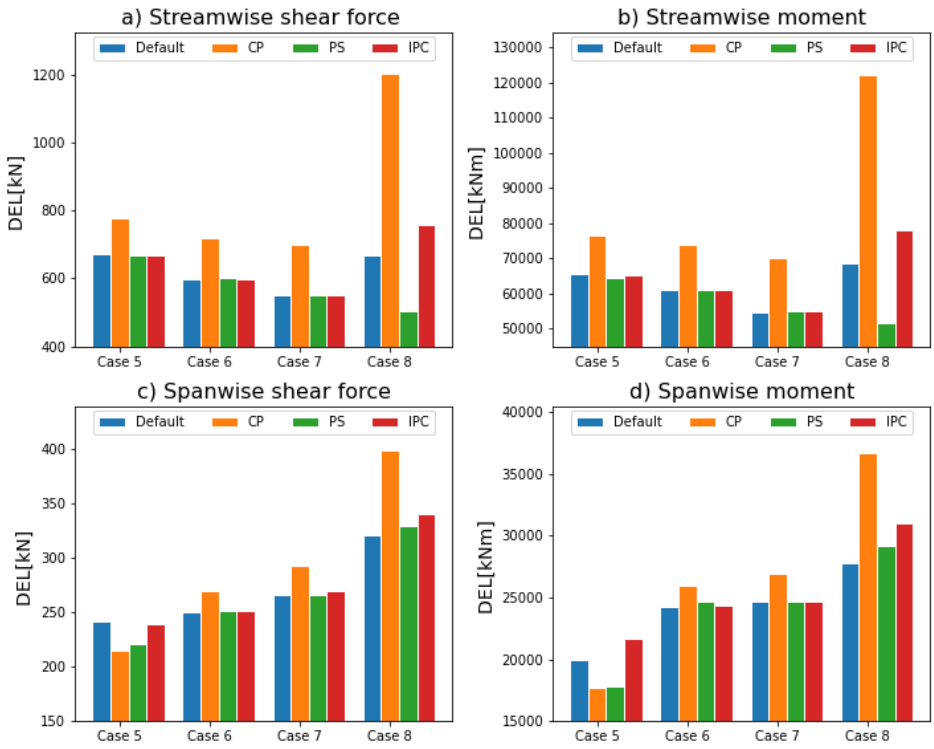

Figure 4.17: Damage equivalent load at the base of the tower.

Tower top

The damage equivalent loads at the tower top are displayed in figure 4.18. CP increases the streamwise shear force in all cases and the streamwise moment in case 8 compared to default. The only load that is reduced by CP is the spanwise shear force in case 5. IPC increases the loads in case 8 and the spanwise loads in case 5 compared to default (collective blade pitch). These are the cases with the most positive and most negative shear. The other two cases are unaffected by IPC. It appears that the PS setting exerts a slight influence on the streamwise shear force in case 8, where it maintains a higher pitch angle.

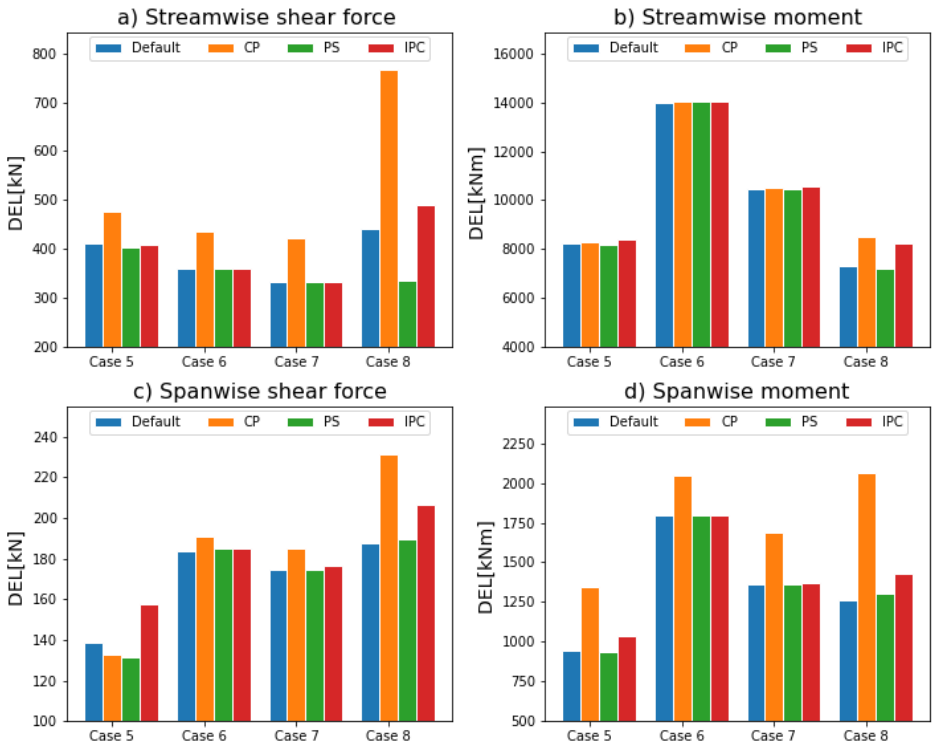

Figure 4.18: Damage equivalent load at the top of the tower.

Blade root

The damage equivalent loads at the blade root are displayed in figure 4.19. Both negative and positive shear cause asymmetric loads, which IPC seems to effectively mitigate. IPC reduces the out-of-plane loads in all cases, except for case 6, where the LLJ is at hub height and the wind profile is symmetric above and under the hub. The in-plane loads at the blade root are more or less constant across all cases, in contrast to the increasing trend observed with increasing LLJ height for the other control strategies. In case 5, where the LLJ is at 90 metres, the in-plane loads are higher with IPC compared to default. CP has higher out-of-plane loads in all cases, and PS has a small reduction in the out-of-plane loads in case 8.

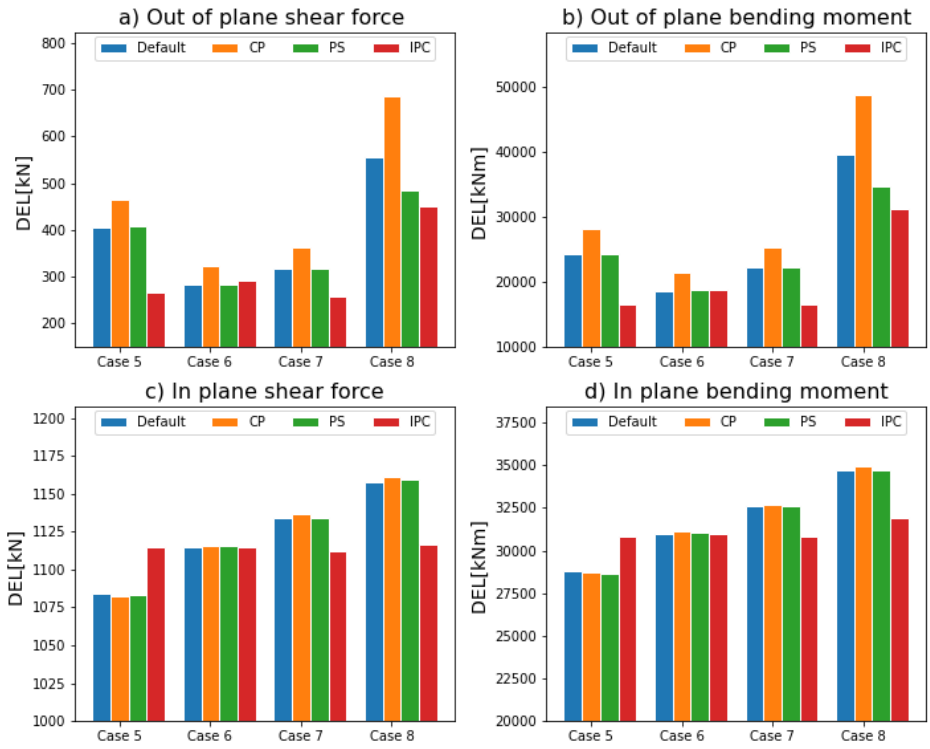

Figure 4.19: Damage equivalent load at the blade root.

4.2.3 Energy production

Figure 4.20 a) and b) illustrate the energy produced and the normalised energy during the 600-second simulation. There are no significant differences in control region 3, but CP is observed to produce slightly less power than the other controllers. CP is designed to minimise fluctuations in power output. When constant generator torque is used, fluctuations in power output are observed in conjunction with fluctuations in wind and wind gusts.

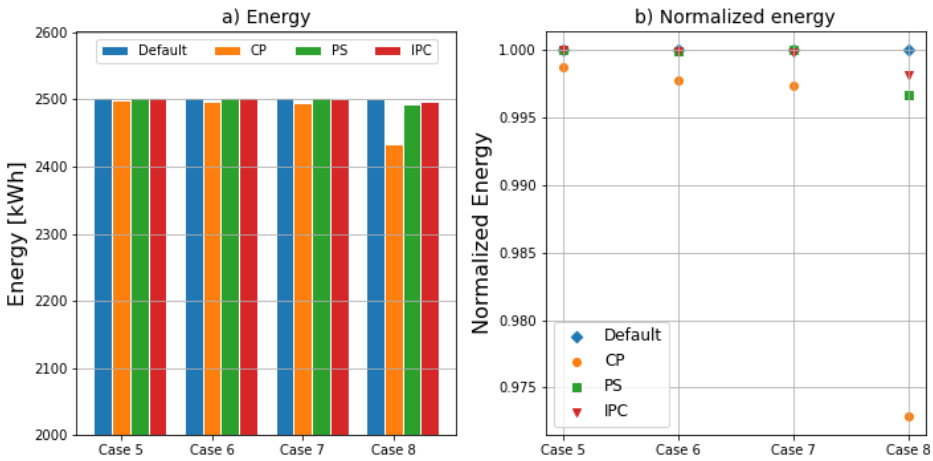

Figure 4.20: Energy produced in 600 seconds for case 5−8.

4.3 Further discussion

In this section, I will undertake further analysis and present a comparative overview of my findings in light of existing studies in the field. The various control strategies demonstrated both positive and negative contributions to the levelized cost of energy (LCOE). Some strategies are effective in reducing load and fatigue, while others increase power. It appears that IPC is the control strategy that mitigates the greatest number of loads without affecting power generation. In particular, out-of-plane fatigue loads at the blade root are significantly reduced by IPC, as evidenced by Santoni et al. (2023) and Lara et al. (2023). However, the spanwise loads by IPC at the tower exhibit varying results depending on the LLJ and control region. The LLJs at 90 metres, which are the only cases where the LLJ core height is below the hub, exhibited an increase in in-plane loads at the blade root. The other LLJ heights exhibited minimal differences in in-plane loads by IPC in control region 2.5, while in control region 3, there was a reduction by IPC. Figure 4.21 shows the power spectral density for the out-of-plane bending moment at the blade root in case 5. This demonstrates that IPC reduces the power at lower frequencies, thereby reducing the 1P loads. This finding is consistent with the results of the study conducted by Bossanyi (2003b). When the LLJ core was at hub height, there were no differences in the fatigue loads as a result of IPC. This was observed in both control

regions 2.5 and 3, as well as for all structural load analysts. This is most likely due to the symmetrical reduction in wind speed above and below the hub. It is also important to consider the additional workload imposed upon the pitch actuator, which is not analysed in this study.

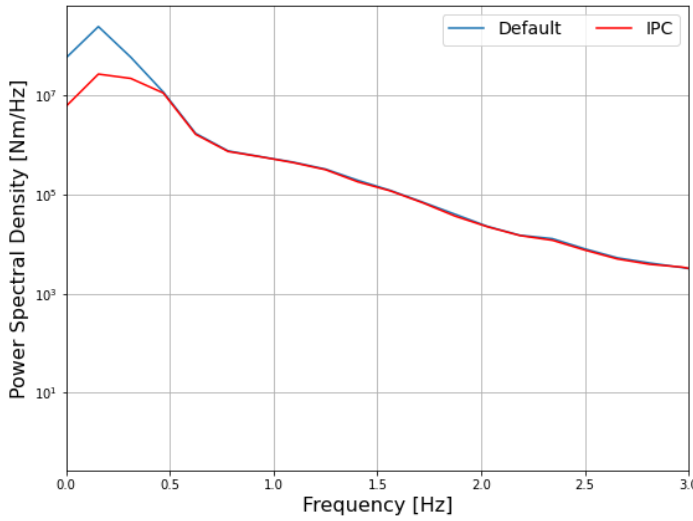

Figure 4.21: Out of plane bending moment load reduction at lower frequencies due to IPC in case 5.

Peak shaving is a control strategy specifically designed to reduce the aerodynamic thrust within control region 2.5, and it is exactly what PS achieves. The higher pitch scheme employed by PS results in a reduction of thrust and torque for all LLJ heights in the control region 2.5. The peaks in thrust are reduced by $10-15\%$, with the greatest reduction occurring in case 2, where the LLJ core height is at hub height. The reduction of the aerodynamic loads also results in a reduction in structural loads on the wind turbine. The streamwise damage equivalent loads at the tower base are significantly reduced, while the spanwise loads at the tower base are mostly reduced in case 1. The reduction in thrust also results in a significant reduction in the out-of-plane loads at the blade root. At the top of the tower, the streamwise shear forces are the only forces that are reduced by PS. One disadvantage of PS is that it captures less power from the wind and generates less power. Furthermore, the amount of peak shaving can be determined by the control engineer. Therefore, the use of PS becomes an equation to try to optimise the levelized cost of electricity. In control region 3, PS only mitig-

ates loads if the pitch angle remains at a higher value when the wind speed dips below a certain threshold. This occurred in case 8, where the mean vertical wind speed was sometimes below this threshold. The peak shaving factor in ROSCO was set to 0.8, which should reduce the maximum thrust by 20%. It is therefore of interest to note that in this study the maximum thrust was reduced by $11-16\%$, and appears to be less reduced than the set value during LLJs. This could also be related to the wind speed and further investigation is required for this hypothesis.

The torque controller CT was included to assess the performance of the default controller, which employs tip speed ratio tracking torque control based on the filtered wind speed at hub height. The default setting is typically the optimal choice for maximizing energy production under rated wind speeds, and it performs well in a typical wind profile. LLJs exhibit greater vertical fluctuations in wind speed than a typical wind profile. This may result in the wind turbine operating at a sub-optimal rotor speed when utilising tip speed ratio tracking torque control. The results demonstrate that under a typical LLJ, the CT controller operates at lower rotor speeds and extracts more power from the wind, resulting in higher energy production. An example of the difference in generator torque and rotor speed is shown in figure 4.22 of case 2. The mean rotor speed for the entire case 2 is 7.41 rpm for the default setting and 7.13 rpm for CT (rated rotor speed is 7.55 rpm). The default controller utilises the filtered wind at hub height, however, the blade tip experiences a different wind speed, resulting in a sub-optimal rotor speed. The smallest variation in energy production occurred in case 1, where the wind speed at the hub height was most accurately aligned with the mean vertical wind speed. As previously demonstrated, a reduction in rotational speed results in a different structural loading. The fatigue loads experienced with CT varies with LLJ height. The out-of-plane loads at the blade root are slightly lower in cases 2 and 3 and higher in cases 1 and 4 compared to the default controller. The streamwise tower loads are lower than the default, except for case 1 where the LLJ is below the hub height. The most notable discrepancy is the spanwise loads at the tower base, which exhibit an increasing trend with increasing LLJ height. This contrasts with the decreasing trend observed in the default controller.

In the above-rated cases, the constant power (CP) strategy was included

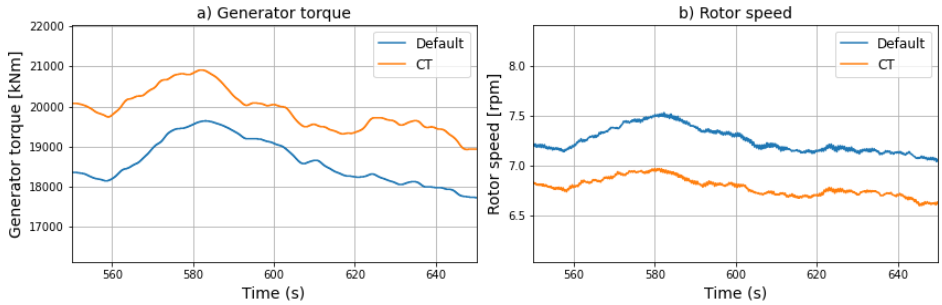

Figure 4.22: 100-second time-series of case 2 that shows the difference in generator torque and rotor speed with (default) and without (CT) TSR tracking torque control.

to check the performance of the default controller which utilises constant torque in control region 3. To maintain a constant power output, CP utilises the rated power as a reference and adjusts the generator torque accordingly. The differences between default and CP generator torque and generator power are illustrated in figure 4.23. CP results in greater fluctuations in thrust and torque, as well as higher maximum values. The tower loads are significantly higher, particularly for the streamwise loads at the tower base. The out-of-plane loads at the blade root are also increased in all cases. The energy production does not differ greatly but is slightly decreased in cases 5 to 7 and decreased by more than 2.5% in case 8. The CP control strategy appears to be sub-optimal due to the increased loads and decreased power. However, the more constant power output may offer advantages in the interaction between the turbine and the electricity grid.

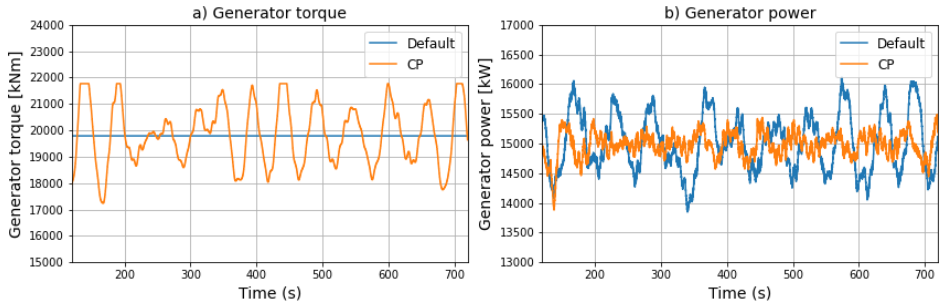

Figure 4.23: 600-second time-series of case 6 that shows the difference in generator torque and power output between default (constant torque above rated) and CP (constant power).

From the perspective of the levelized cost of electricity, it is evident that an increase in electricity production with CT is beneficial. The operational and maintenance costs should be kept to a minimum by reducing the wear and tear. The implementation of individual pitch control has the beneficial effect of reducing the structural loads on the blades. However, this approach also increases the wear and tear on the pitch actuators. It can be concluded that a reduction in fatigue loads through the use of PS over several decades will also be highly beneficial, with the potential to extend the lifetime of the wind turbine. Determining which of these strategies is the most beneficial is challenging. This demands the collation of operational data and costs.

Limitations

The analysis conducted in this study was performed on behalf of the OpenFAST simulation of the IEA 15MW reference wind turbine. The objective of this study was to identify the differences between the control strategies, rather than to assess the values themselves. Consequently, the results cannot be used to determine the actual loads that a real turbine would experience. The same applies to power production.

Chapter 5

Conclusions and Future Work

This thesis has investigated the performance of different control strategies on a 15MW floating offshore wind turbine during Low-Level Jet (LLJ) events. The performance was evaluated in terms of energy production, structural loads and aerodynamic loads. Individual Pitch Control (IPC), Peak Shaving (PS), Tip Speed Ratio (TSR) tracking torque control, torque control without TSR tracking, and Constant Power (CP) tracking torque control were all studied under a variety of LLJ wind profiles. Both ideal and real observations of LLJs were included in the study.

The findings indicated that the control strategy has a significant impact on the performance of the wind turbine. IPC was the control strategy that mitigates the greatest number of loads without affecting power generation. In particular, the out-of-plane loads at the blade root were reduced by IPC, although when the LLJ core height was at hub height (150m), IPC did not provide any advantages.

Peak shaving was the control strategy that reduced both the mean and the maximum aerodynamic loads and mitigated particularly the streamwise fatigue loads well in control region 2.5. PS was not influenced to the same extent by the height of the LLJ as the other control strategies. The streamwise loads at the tower base and the streamwise shear force at the tower top remained relatively consistent at all LLJ heights in control region 2.5. The other control strategies exhibited variation with LLJ height, particularly in the case where the LLJ core height was 90 metres. However, PS did result in a significant reduction in energy production.

The tip speed ratio tracking torque control, which is typically employed

to optimise energy production below-rated wind speed, has been demonstrated to exhibit suboptimal performance during a typical LLJ. The tip speed ratio is calculated based on the estimated wind speed at hub height. As a result, it becomes challenging to optimize the rotor speed with the LLJ wind profile, which varies considerably in the vertical direction. When the tip speed ratio tracking component of torque control was deactivated, the wind turbine was observed to extract more power from the wind and operate at slightly lower rotor speeds. The increase in power without TSR tracking torque had a different impact on the fatigue loads depending on the LLJ height and load direction.

The constant power torque controller exhibited higher maximum aerodynamic loads and generally higher fatigue loads than the constant torque configuration in control region 3. Furthermore, constant power did not provide any benefits during low-level jets.

It appears that control strategies during low-level jets have not been widely researched or published in the academic literature. This study has investigated the performance and impact of some control strategies individually. It would be of interest in the future to observe the performance of several control strategies used in combination during a low-level jet. Furthermore, it is recommended that research be conducted to identify the optimal rotor speed to the LLJ profile and height when the wind turbine is operating below rated wind speed. To achieve this in the field, effective methods must be developed to estimate the wind field over the entire rotor. It would be beneficial for future studies to include a greater number of observed LLJs to gain a more comprehensive understanding of turbine performance. Further studies should be conducted on wind farms, focusing on the performance of multiple turbines combined during low-level jets.

Bibliography

Abbas, N., Zalkind, D., Pao, L., & Wright, A. (2021). A reference open-source controller for fixed and floating offshore wind turbines. *Wind Energy Science Discussions*, *2021*, 1–33. URL: https://wes.copernicus.org/preprints/wes-2021-19/. doi:10.5194/wes-2021-19.

Abbas, N. J., Zalkind, D. S., Pao, L., & Wright, A. (2022). A reference open-source controller for fixed and floating offshore wind turbines. *Wind Energy Science*, *7*, 53–73.

Ahmed, F. (2024). Structural dynamics. https://github.com/FM-Ahmed/Structural-dynamics. Accessed on: 13.05.2024.

Ahmed, F. M. (2023). *Low-level jet height's impact on wind turbine loads: A case study*. Master's thesis The University of Bergen.

Ahmed, F. M., & Paskyabi, M. B. (2023). Effects of negative shear on loads for a 15 mw offshore wind turbine during low-level jet events. In *Journal of Physics: Conference Series* (p. 012046). IOP Publishing volume 2626.

Aho, J., Buckspan, A., Laks, J., Fleming, P., Jeong, Y., Dunne, F., Churchfield, M., Pao, L., & Johnson, K. (2012). A tutorial of wind turbine control for supporting grid frequency through active power control. In *2012 American Control Conference (ACC)* (pp. 3120–3131). IEEE.

Allen, C., Viscelli, A., Dagher, H., Goupee, A., Gaertner, E., Abbas, N., Hall, M., & Barter, G. (2020). *Definition of the UMaine VolturnUS-S reference platform developed for the IEA wind 15-megawatt offshore reference wind turbine*. Technical Report National Renewable Energy Lab.(NREL), Golden, CO (United States); Univ. of ....

Bakhoday-Paskyabi, M., Bui, H., & Mohammadpour Penchah, M. (2022). Atmospheric-wave multi-scale flow modelling, deliverable d2. 1 for 385 hiperwind project.

Bakhoday-Paskyabi, M., & Flügge, M. (2021). Predictive capability of wrf cycling 3dvar: Lidar assimilation at fino1. In *Journal of Physics: Conference Series* (p. 012006). IOP Publishing volume 2018.

Bhattacharya, S. (2019). *Design of foundations for offshore wind turbines*. John Wiley & Sons.

Blackadar, A. K. (1957). Boundary layer wind maxima and their significance for the growth of nocturnal inversions. *Bulletin of the American Meteorological Society*, *38*, 283–290.

Bonner, W. D. (1968). Climatology of the low level jet. *Monthly Weather Review*, *96*, 833–850.

Bossanyi, E. (2003a). Wind turbine control for load reduction. *Wind Energy: An International Journal for Progress and Applications in Wind Power Conversion Technology*, *6*, 229–244.

Bossanyi, E. A. (2003b). Individual blade pitch control for load reduction. *Wind Energy: An International Journal for Progress and Applications in Wind Power Conversion Technology*, *6*, 119–128.

Bouckaert, S., Pales, A. F., McGlade, C., Remme, U., Wanner, B., Varro, L., D'Ambrosio, D., & Spencer, T. (2021). Net zero by 2050: A roadmap for the global energy sector, .

Carter, D. (1982). Prediction of wave height and period for a constant wind velocity using the jonswap results. *Ocean Engineering*, *9*, 17–33.

Cheynet, E., Jakobsen, J. B., & Reuder, J. (2018). Velocity spectra and coherence estimates in the marine atmospheric boundary layer. *Boundary-layer meteorology*, *169*, 429–460.

Davenport, A. G. (1961). The spectrum of horizontal gustiness near the ground in high winds. *Quarterly Journal of the Royal Meteorological Society*, *87*, 194–211.

De Jong, E., Quon, E., & Yellapantula, S. (2024). Mechanisms of low-level jet formation in the us mid-atlantic offshore. *Journal of the Atmospheric Sciences*, *81*, 31–52.

DNV (2024). Wind turbine design software: Bladed. retrieved from. URL: https://www.dnv.com/services/wind-turbine-design-software-bladed-3775/ accessed: 2024-03-27.

Dnv, G. (2014). Dnv-os-j101–design of offshore wind turbine structures. *DNV GL: Oslo, Norway*, .

European Commission (2023). Eu wind power action plan: Keep wind power a european success story. URL: https://commission.europa.eu/news/eu-wind-power-action-plan-keep-wind-power-european-success-story-2023-10-24_en accessed on: 2024-02-09.

Frandsen, S., & Christensen, C. (1994). Structural loads in large wind farm arrays. In *Contributions from the Department of Meteorology and Wind Energy to the EWEC'94 Conference in Thessaloniki, Greece*.

Freebury, G., & Musial, W. (2000). Determining equivalent damage loading for full-scale wind turbine blade fatigue tests. In *2000 ASME wind energy symposium* (p. 50).

Gaertner, E., Rinker, J., Sethuraman, L., Zahle, F., Anderson, B., Barter, G. E., Abbas, N. J., Meng, F., Bortolotti, P., Skrzypinski, W., Scott, G. N., Feil, R., Bredmose, H., Dykes, K., Shields, M., Allen, C., & Viselli, A. (2020a). Iea wind tcp task 37: Definition of the iea 15-megawatt offshore reference wind turbine, . URL: https://www.osti.gov/biblio/1603478. doi:10.2172/1603478.

Gaertner, E., Rinker, J., Sethuraman, L., Zahle, F., Anderson, B., Barter, G. E., Abbas, N. J., Meng, F., Bortolotti, P., Skrzypinski, W. et al. (2020b). *IEA wind TCP task 37: definition of the IEA 15-megawatt offshore reference wind turbine*. Technical Report National Renewable Energy Lab.(NREL), Golden, CO (United States).

Garratt, J. R. (1994). The atmospheric boundary layer. *Earth-Science Reviews*, *37*, 89–134.

Gutierrez, W., Ruiz-Columbie, A., Tutkun, M., & Castillo, L. (2017). Impacts of the low-level jet's negative wind shear on the wind turbine. *Wind energy science*, *2*, 533–545.

Hasselmann, K., Barnett, T. P., Bouws, E., Carlson, H., Cartwright, D. E., Enke, K., Ewing, J., Gienapp, A., Hasselmann, D., Kruseman, P. et al. (1973). Measurements of wind-wave growth and swell decay during the joint north sea wave project (jonswap). *Ergaenzungsheft zur Deutschen Hydrographischen Zeitschrift, Reihe A*, .

Holton, J. R. (1967). The diurnal boundary layer wind oscillation above sloping terrain. *Tellus*, *19*, 200–205.

International Renewable Energy Agency (2023). *Renewable power generation costs in 2022*. Abu Dhabi: International Renewable Energy Agency. URL: https://mc-cd8320d4-36a1-40ac-83cc-3389-cdn-endpoint.azureedge.net/-/media/Files/IRENA/Agency/Publication/2023/Aug/IRENA_Renewable_power_generation_costs_in_2022.pdf?rev=cccb713bf8294cc5bec3f870e1fa15c2.

Johnson, K. E. (2004). *Adaptive torque control of variable speed wind turbines*. University of Colorado at Boulder.

Jonkman, J. M., Buhl, M. L. et al. (2005). *FAST user's guide* volume 365. National Renewable Energy Laboratory Golden, CO, USA.

Kaimal, J. C., & Finnigan, J. J. (1994). *Atmospheric boundary layer flows: their structure and measurement*. Oxford university press.

Kaimal, J. C., Wyngaard, J., Izumi, Y., & Coté, O. (1972). Spectral characteristics of surface-layer turbulence. *Quarterly Journal of the Royal Meteorological Society*, *98*, 563–589.

Kundu, P. K., Cohen, I. M., & Dowling, D. R. (2015). *Fluid mechanics*. Academic press.

Lara, M., Mulders, S. P., van Wingerden, J.-W., Vázquez, F., & Garrido, J. (2023). Analysis of adaptive individual pitch control schemes for blade fatigue load reduction on a 15 mw wind turbine. *Applied Sciences*, *14*, 183.

Matsuishi, M., & Endo, T. (1968). Fatigue of metals subjected to varying stress. *Japan Society of Mechanical Engineers, Fukuoka, Japan*, *68*, 37–40.

Meyers, J., Bottasso, C., Dykes, K., Fleming, P., Gebraad, P., Giebel, G., Göçmen, T., & Van Wingerden, J.-W. (2022). Wind farm flow control: prospects and challenges. *Wind Energy Science Discussions*, *2022*, 1–56.

Miles, J. W. (1957). On the generation of surface waves by shear flows. *Journal of Fluid Mechanics*, *3*, 185–204.

Moriarty, P. J., & Hansen, A. C. (2005). *AeroDyn theory manual*. Technical Report National Renewable Energy Lab., Golden, CO (US).

Niebsch, J., Ramlau, R., & Nguyen, T. T. (2010). Mass and aerodynamic imbalance estimates of wind turbines. *Energies*, *3*, 696–710.

Nielsen, F. G. (2024). *Offshore Wind Energy: Environmental Conditions and Dynamics of Fixed and Floating Turbines*. Cambridge University Press.

Ning, S. (2013). *CCBlade Documentation: Release 0.1. 0*. Technical Report National Renewable Energy Lab. (NREL), Golden, CO (United States).

Njiri, J. G., & Söffker, D. (2016). State-of-the-art in wind turbine control: Trends and challenges. *Renewable and Sustainable Energy Reviews*, *60*, 377–393.

NREL (2021). ROSCO. Version 2.4.1. URL: https://github.com/NREL/ROSCO.

NREL (2023). OpenFAST Documentation. https://openfast.readthedocs.io/en/main/source/user/index.html#. Accessed on: 2024-04-03.

Phillips, O. M. (1957). On the generation of waves by turbulent wind. *Journal of fluid mechanics*, *2*, 417–445.

Pielke, R., & Panofsky, H. (1970). Turbulence characteristics along several towers. *Boundary-Layer Meteorology*, *1*, 115–130.

Pöschke, F., & Schulte, H. (2021). Model-based control of wind turbines for active power control: A unified sector-nonlinearity approach based on takagi-sugeno modeling. *at-Automatisierungstechnik*, *69*, 820–835.

Ragheb, M. (2014). Optimal rotor tip speed ratio. *Lecture notes of Course no. NPRE*, *475*.

Ross, H., Hall, M., Herber, D. R., Jonkman, J., Sundarrajan, A. K., Tran, T. T., Wright, A., Zalkind, D., & Johnson, N. (2022). Development of a control co-design modeling tool for marine hydrokinetic turbines. In *ASME International Mechanical Engineering Congress and Exposition* (p. V006T08A067). American Society of Mechanical Engineers volume 86687.

Santoni, C., Khosronejad, A., Seiler, P., & Sotiropoulos, F. (2023). Toward control co-design of utility-scale wind turbines: Collective vs. individual blade pitch control. *Energy Reports*, *9*, 793–806.

Suresh, S. (1998). *Fatigue of materials*. Cambridge university press.

Tang, S., Tian, D., Fang, J., Liu, F., & Zhou, C. (2021). Individual pitch controller characteristics analysis and optimization under aerodynamic imbalanced loads of wind turbines. *Energy Reports*, *7*, 6489–6500.

Voutsinas, S. G. (2010). Structural dynamics of wind turbines. *Wind Power Generation and Wind Turbine Design*, (pp. 121–151).

Wagner, D., Steinfeld, G., Witha, B., Wurps, H., & Reuder, J. (2019). Low level jets over the southern north sea, .

Wang, L., Bergua, R., Robertson, A., Wright, A., Zalkind, D., Fowler, M., Lenfest, E., Viselli, A., Goupee, A., & Kimball, R. (2024). Experimental investigation of advanced turbine control strategies and load-mitigation measures with a model-scale floating offshore wind turbine system. *Applied Energy*, *355*, 122343.

Zhang, X., Yang, C., & Li, S. (2019). Influence of low-level jet intensity on aerodynamic loads of horizontal axis wind turbine rotor. *Engineering Applications of Computational Fluid Mechanics*, *13*, 300–308.